# Electrostatic modes of ion-trap plasmas

J. J. Bollinger, D. J. Heinzen,* F. L. Moore,* Wayne M. Itano, and D. J. Wineland
*Time and Frequency Division, National Institute of Standards and Technology, Boulder, Colorado 80303*

Daniel H. E. Dubin
*Department of Physics, University of California at San Diego, La Jolla, California 92093*
(Received 4 January 1993)

The electrostatic modes of a non-neutral plasma confined in a Penning or Paul (rf) trap are discussed in the limit that the Debye length is small compared to the plasma dimensions and the plasma dimensions are small compared to the trap dimensions. In this limit the plasma shape is spheroidal and analytic solutions exist for all of the modes. The solutions for the modes of a Paul-trap plasma are a special case of the modes of a Penning-trap plasma. A simple derivation of some of the low-order quadrupole modes is given. Experimental measurements of these mode frequencies on plasmas of laser-cooled $Be^+$ ions in a Penning trap agree well with the calculations. A general discussion of the higher-order modes is given. The modes provide a nondestructive method for obtaining information on the plasma density and shape. In addition, they may provide a practical limit to the density and number of charged particles that can be stored in a Penning trap.

PACS number(s): 32.80.Pj, 32.90.+a, 52.25.Wz, 52.35.Fp

## I. INTRODUCTION

Penning traps [1,2] typically use a uniform magnetic field superimposed along the axis of azimuthally symmetric electrodes to confine charged particles. Radial confinement is provided by the axial magnetic field and axial confinement is provided by electrostatic potentials applied to the trap electrodes (see Fig. 1). Paul (rf) traps [1] use an electrode structure similar to Penning traps, but there is no magnetic field, and a combination of rf and electrostatic potentials are applied to trap electrodes. Charged particles are confined by the inhomogeneous rf fields (the pondermotive force) to a region of minimum rf field strength near the trap center. Penning and Paul traps are used in a number of studies on charged atomic particles such as mass spectroscopy [3–8], high-precision magnetic-moment measurements [1,9,10], high-resolution spectroscopy and frequency standards [1,11–14], charge-transfer studies [15], non-neutral-plasma studies [2,16–21], and antimatter storage [7,22–24]. In many of these experiments more than one charged atomic particle (a "cloud") are stored in the trap and cooled to low temperatures. A cloud of charged particles in a Penning trap can be considered a plasma, in particular a non-neutral plasma, when the Debye length is less than the cloud dimensions. This paper discusses the electrostatic modes of these plasmas in the limit that the Debye length is much less than the plasma dimensions and when the plasma dimensions are small compared to the trap dimensions. As discussed below, the modes of a Paul-trap plasma are described by a special case of the Penning-trap plasma modes. Therefore in this paper we concentrate our discussion on the modes of Penning-trap plasmas and show how solutions for the modes of an rf-trap plasma follow from the Penning-trap results.

Measurement of the plasma mode frequencies may have applications for ion trap experiments. For example, mass spectroscopy experiments done with a cloud or plasma of ions in a Penning trap can have systematic shifts associated with the distances of the ions from the trap center and the small anharmonicities of the trapping po-

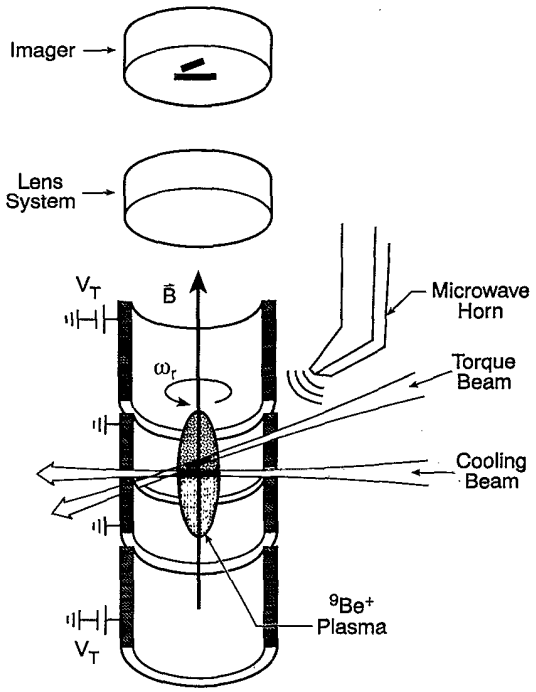


FIG. 1. Sketch of a Penning trap used to make mode measurements on a plasma of $^9Be^+$ ions. The size of the plasma is exaggerated. The trap electrodes (shown in cross section) are right circular cylinders with inner radius $\rho_0=1.27$ cm. They provide a quadratic potential near the trap center with $A_2=0.236$. Some other Penning traps use hyperboloids of revolution as trap electrodes. The laser beams, microwave horn, and imaging system are used in the measurement of the plasma modes as described in Sec. IV.


Work of the U. S. Government
Not subject to U. S. copyright

tential [6,25,26]. In high-resolution atomic spectroscopy of ions in a Penning trap, one of the largest systematic shifts is the second-order Doppler shift associated with the $\mathbf{E}\times\mathbf{B}$ rotation of the ions about the magnetic field axis of the trap [12]. The larger the radius of the plasma, the larger the second-order Doppler shift. A third application is illustrated by experiments which measure electron-ion recombination by passing an electron beam through a sample of ions trapped in a Penning trap [27]. In these studies, it would be desirable to have a direct knowledge of the geometrical overlap of the electron beam with the ion sample. In all of the above examples, the plasma shape and density, along with the number of trapped ions, determine the radial and axial positions of the ions and therefore the size of the required corrections. Similar considerations apply to experiments on ions in a Paul trap. In some cases the plasma shape and density can be determined with a laser [20,28]. When this or other techniques are not available, detection of the plasma modes, perhaps through induced image currents in the trap electrodes, could provide this information.

Recent experiments have trapped positron [23] and antiproton [7,24] plasmas in Penning traps. The current techniques for obtaining information about these plasmas involves ejecting the plasma from the trap. Detection of the plasma modes should provide a nondestructive diagnosis for obtaining information on the antimatter plasma density, temperature, and shape. A goal of the antimatter work is the high-density storage of large numbers of positrons and antiprotons for transport to different laboratories around the world. Field errors in the trapping potential can excite plasma modes and enhance radial transport. Excitation of the plasma modes may therefore set a practical limit on the density and number of antiparticles that can be stored in a Penning trap.

In addition to having potential applications to current experiments, the electrostatic modes of a Penning-trap plasma may also provide a tool for studying the dynamics of non-neutral and strongly coupled plasmas. A simple, analytic form has been obtained for all of the electrostatic modes of a low-temperature Penning-trap plasma [29]. This is the only finite length geometry for which exact mode eigenfrequencies and eigenfunctions have been calculated. Therefore the Penning trap may provide an interesting geometry for the study of plasma modes and their importance to the dynamical behavior of non-neutral plasmas. For example, it should be possible to study how errors in the trapping fields couple to the plasma modes and enhance radial transport [19]. Measurement of the damping of the modes should provide information on the plasma's viscosity. This measurement could presumably be done with a strongly correlated plasma over a range of magnetic field strengths where very little information is available.

In Sec. II we review the static properties of a cold, Penning-trap plasma in thermal equilibrium. We assume the trapped particle number $N\gg 1$. For sufficiently low temperature or small Debye length, the plasma has constant density. If the plasma dimensions are small compared to the trap electrode dimensions, then the confining potential may be assumed to be quadratic and the effect of image charges neglected. In this case, the plasma has a spheroidal boundary with an aspect ratio determined by the plasma density and the axial restoring force of the trap. This is the starting point for describing and calculating the modal excitations of a plasma in thermal equilibrium. In Sec. III we describe a simple but exact calculation for some of the quadrupole modes of a spheroidal Penning-trap plasma. We show how these modes could be used to measure the density and shape of a Penning-trap plasma. Section IV compares the results of the quadrupole mode calculations with measurements [21] done on about 2000 laser-cooled $^9Be^+$ ions in a Penning trap. In that section we show how a zero-frequency quadrupole mode was excited by a misalignment of the magnetic field axis with respect to the electrostatic symmetry axis of the trap. Excitation of this mode tended to limit the plasma density. Section V discusses the higher-order modes of a Penning-trap plasma [29]. Modes that can be excited by static field errors are identified.

## II. STATIC PROPERTIES

The Penning trap shown in Fig. 1 consists of four cylindrical electrodes. The outer cylinders are called the "end-cap" electrodes in analogy with the end caps of a hyperbolic Penning trap [1]. The inner cylinders are electrically shorted and together called the "ring" electrode. With a positive potential $V_T$ applied to the end-cap electrodes with respect to the ring electrode, positively charged particles (ions) can be electrostatically confined in the direction of the trap axis. A static, uniform magnetic field $\mathbf{B}=B\hat{\mathbf{z}}$ parallel to the trap's symmetry axis confines the ions in the radial direction. Near the center of the trap, where the ions are confined, the radial component of the trap electric field is directed outward. This field produces an $\mathbf{E}\times\mathbf{B}$ circular drift of the ions about the symmetry axis of the trap. As the ions rotate through the magnetic field, they experience a Lorentz force directed radially inward.

With sufficiently long confinement, the ions evolve to a state of thermal equilibrium characterized by a uniform "rigid" rotation of the ions at a frequency $\omega_r$ [18,28,30]. Specifically, the rotation frequency $\omega_r$ is independent of radius. In the limit of zero temperature, the plasma density $n_0$ and plasma frequency $\omega_p$ are constant in the plasma interior and drop abruptly to 0 at the plasma edge. The density depends on the rotation frequency according to (Système International units are used throughout)

$$n_0=\frac{2\epsilon_0 m\omega_r(\Omega-\omega_r)}{q^2}\ , \tag{2.1}$$

where $\Omega=qB/m$ is the ion cyclotron frequency, $q$ and $m$ are the charge and mass of the ion, and $\epsilon_0$ is the permittivity of the vacuum. The plasma frequency is therefore related to the rotation frequency through the equation

$$\omega_p^2\equiv\frac{q^2n_0}{\epsilon_0 m}=2\omega_r(\Omega-\omega_r)\ . \tag{2.2}$$

In this paper we use the convention that the symbols $\omega_r$

and $\Omega$ denote positive quantities. However, for positive ions, the sense of the rotation and the sense of the cyclotron motion with respect to **B** are actually negative. Specifically, when viewed from above the $x$-$y$ plane, the ions move in clockwise orbits. For nonzero temperatures, the density drops to 0 at the plasma edge in a distance on the order of a Debye length $\lambda_D$ [18,30], where

$$\lambda_D = \left[\frac{\epsilon_0 kT}{n_0 q^2}\right]^{1/2}, \tag{2.3}$$

$k$ is Boltzmann's constant, and $T$ is the ion temperature. For $\lambda_D \ll$ (plasma dimensions), the plasma therefore has a uniform density, given by Eq. (2.1), with sharp boundaries. For very low temperatures, there are correlations in the ion positions [20,31,32], and the ion density is not constant over length scales small compared to the interion spacing ($\sim n_0^{-1/3}$). However, as long as the interion spacing is small compared to the plasma dimensions (that is, as long as the number of ions $N \gg 1$) and small compared to the wavelength of the plasma modes, the plasma can be treated as a constant-density plasma even in the presence of spatial correlations.

The plasma boundary has a simple shape in the limit that the plasma dimensions are small compared to the trap dimensions [28,33]. Near its center, the electrostatic potential of the trap, relative to the potential at the trap center, can be written as

$$\phi_T(r,z) = \frac{m\omega_z^2}{4q}(2z^2 - r^2), \tag{2.4}$$

where $r$ and $z$ are cylindrical coordinates, and $\omega_z$ is the frequency at which a single trapped ion (or the center-of-mass of a cloud of ions) oscillates along the $z$ axis. For the cylindrical trap of Fig. 1,

$$\omega_z = \left[\frac{4qV_T A_2}{m\rho_0^2}\right]^{1/2}, \tag{2.5}$$

where $\rho_0$ is the inner radius of the trap electrodes and $A_2$ is a dimensionless parameter that depends on the geometry of the trap design. For the trap of Fig. 1, $A_2 = 0.236$. In general, the total electrostatic potential is the sum of the trap potential, the space-charge potential of the ions, and a potential due to the induced image charges on the trap electrodes. If the plasma dimensions are much less than the trap dimensions, the trap potential over the region of the plasma is given by Eq. (2.4), and the effect of the induced image charges can be neglected. In this case the shape of the plasma boundary is a spheroid (an ellipsoid of revolution) as shown in Fig. 2 [28,33]. Let $2r_0$ and $2z_0$ denote the diameter and the axial extent of the plasma as shown in Fig. 2. The plasma aspect ratio $\alpha \equiv z_0/r_0$ is related [28] to the plasma frequency $\omega_p$ and the trap axial frequency $\omega_z$ by

$$\frac{\omega_z^2}{\omega_p^2} = Q_1^0\left[\frac{\alpha}{(\alpha^2-1)^{1/2}}\right] \Big/ (\alpha^2-1), \tag{2.6}$$

where $Q_l^m$ is the associated Legendre function of the second kind [34]. When the plasma is a prolate spheroid

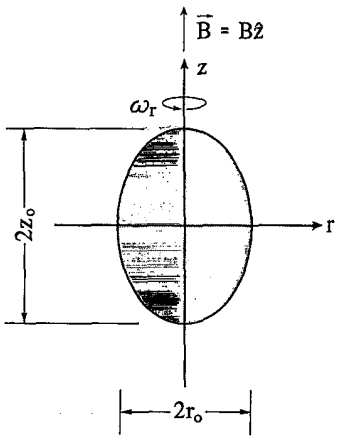


FIG. 2. Spheroidal shape of a Penning-trap plasma. This shape is obtained under the conditions of thermal equilibrium and $\lambda_D \ll$(plasma dimensions) $\ll$(trap dimensions).

($\alpha > 1$), Eq. (2.6) can be written as

$$\frac{\omega_z^2}{\omega_p^2} = \frac{1}{\alpha^2-1}\left[\frac{u_p}{2}\ln\left[\frac{u_p+1}{u_p-1}\right]-1\right], \quad u_p \equiv \frac{\alpha}{(\alpha^2-1)^{1/2}}. \tag{2.7}$$

When the plasma is an oblate spheroid ($\alpha < 1$), Eq. (2.6) can be written as

$$\frac{\omega_z^2}{\omega_p^2} = \frac{1}{\alpha^2-1}\left[u_0 \tan^{-1}\left[\frac{1}{u_0}\right]-1\right], \quad u_0 \equiv \frac{\alpha}{(1-\alpha^2)^{1/2}}. \tag{2.8}$$

Figure 3 shows a graph of $\omega_z^2/\omega_p^2$ versus the plasma aspect ratio $\alpha$. Experimental measurements of $\omega_z, \omega_p$, and $\alpha$ discussed in Ref. [28] are in good agreement with the

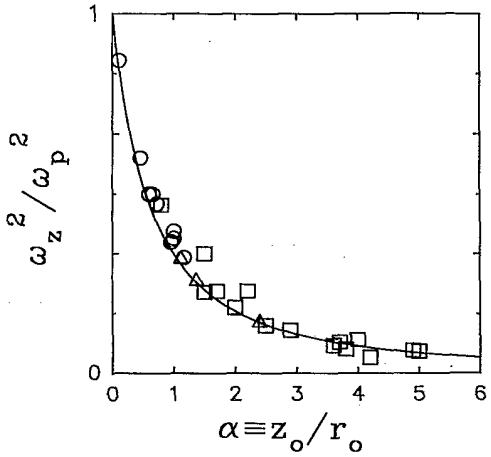


FIG. 3. Relationship between the plasma aspect ratio $\alpha$ and $\omega_z^2/\omega_p^2$ for spheroidal-shaped plasmas in a Penning trap. The solid line is a theoretical curve from Eq. (2.6) with no adjustable parameters. The experimental measurements, described in Ref. [28], were taken with two different traps at three different axial frequencies between $\omega_z/\Omega = 0.071$ and 0.121.

theoretical calculation of Eq. (2.6).

In the next section the potential inside a uniformly charged spheroid (the space-charge potential of a cold Penning-trap plasma) will be used to calculate some of the quadrupole mode frequencies. For $r,z$ inside the plasma, the space-charge potential $\phi_I$ can be written [28,33,35] as

$$\phi_I(r,z)=-\frac{m\omega_p^2}{6q}[a(\alpha)r^2+b(\alpha)z^2]\ , \tag{2.9}$$

where $\alpha$ is the plasma aspect ratio, $\omega_p$ is the plasma frequency given by Eq. (2.2), $b(\alpha)=3Q_1^0(\alpha/(\alpha^2-1)^{1/2})/(\alpha^2-1)$, and Poisson's equation requires $2a(\alpha)+b(\alpha)=3$. A spherical plasma has $a=b=1$. At the limit $b=3$, the aspect ratio $\alpha=0$, and the plasma is an infinitely thin disk. (Because we require $z_0\gg\lambda_D$, here infinitely thin means $z_0\ll r_0$.) With $a=\frac{3}{2}$, the aspect ratio $\alpha$ is infinite, and the plasma is an infinitely long cylindrical column ($z_0\gg r_0$). In Eq. (2.9) we choose the potential at the center of the spheroid to be 0. If the potential is chosen to be 0 at $\infty$, then Eq. (2.9) neglects a term which depends on the plasma aspect ratio $\alpha$ but is independent of $r$ and $z$.

It is instructive to consider the plasma equilibrium as a function of rotation frequency $\omega_r$ for fixed trapping conditions (fixed $\omega_z$, $\Omega$, and $N$). Constant density equilibria exist for $\omega_z<\Omega/\sqrt{2}$ and $\omega_m<\omega_r<\Omega-\omega_m$, where

$$\omega_m=\Omega/2-(\Omega^2/4-\omega_z^2/2)^{1/2} \tag{2.10}$$

is a single-ion magnetron frequency [1]. For $\omega_r$ slightly larger than $\omega_m$, $\omega_z^2/\omega_p^2\simeq 1$, and the plasma is shaped like a pancake (an oblate spheroid). In the limit that $\omega_r\to\omega_m$, the plasma's aspect ratio $\alpha\to 0$, and the plasma's radius $r_0\to\infty$. As $\omega_r$ increases, $\omega_z^2/\omega_p^2$ decreases and the plasma's aspect ratio $\alpha$ increases by decreasing $r_0$ and increasing $z_0$. At $\omega_r=\Omega/2$ the plasma attains its maximum aspect ratio (smallest $r_0$ and largest $z_0$) and maximum density $n_B=\epsilon_0 m\Omega^2/2q^2$. The condition $\omega_r=\Omega/2$ is often called Brillouin flow [36]. In a frame of reference rotating with the plasma, the motion of an individual ion within the non-neutral plasma consists of circular gyrations (perturbed cyclotron orbits) at the frequency $\Omega-2\omega_r$. At Brillouin flow, these gyrating orbits become free streaming (straight-line trajectories), and the plasma behaves in many ways like an unmagnetized plasma [36]. Therefore at $\omega_r=\Omega/2$, a Penning-trap plasma behaves dynamically like a plasma confined in an rf (Paul) trap (neglecting the rf micromotion). As $\omega_r$ increases beyond $\Omega/2$, the plasma's aspect ratio $\alpha$ and density $n_0$ decrease. Because $n_0$ is an even function of $\omega_r$ about $\omega_r=\Omega/2$ [see Eq. (2.1)], the plasma's aspect ratio, radius, and axial extent are even functions of $\omega_r$ about $\omega_r=\Omega/2$. Figure 4 shows a graph of the radius of a plasma of $^9Be^+$ ions as a function of rotation frequency. The plasma's rotation frequency and radius were measured with techniques described in Sec. IV. Good agreement was obtained between the observed and predicted dependence of the plasma's radius on rotation frequency.

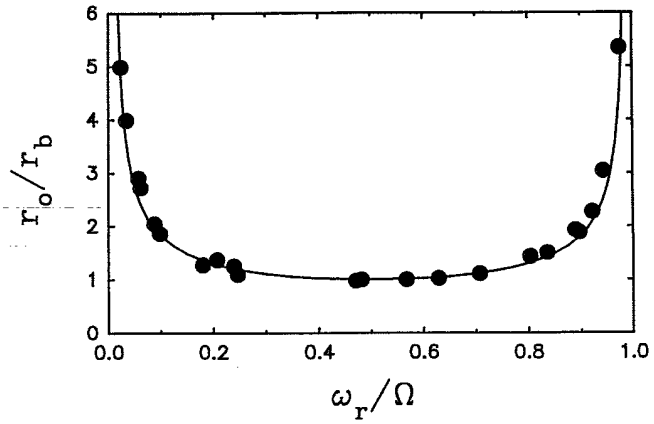


FIG. 4. Radius $r_0$ of a plasma of $\simeq 2000$ $^9Be^+$ ions as a function of rotation frequency $\omega_r$. The radius is plotted in units of $r_b$, the plasma radius at the Brillouin limit, and the rotation frequency is plotted in units of the cyclotron frequency $\Omega$. The solid line is a theoretical curve involving no adjustable parameters. The data were taken as described in Sec. IV with $\Omega/2\pi=1.4$ MHz and $\omega_z/\Omega=0.151$.

With the assumption of thermal equilibrium and max $(\lambda_D,\ n_0^{-1/3})\ll$ (plasma dimensions) $\ll$ (trap dimensions), a Penning-trap plasma has uniform density with a spheroidal boundary. Modal excitations on this equilibrium can be conveniently described with spheroidal coordinates by two integers $(l,m)$ with $l\geq 1$ and $m\geq 0$ [29]. (Negative integral values of $m$ are allowed, but do not give rise to new modes.) The index $m$ denotes an azimuthal dependence $e^{im\phi}$ of the plasma mode potential. The index $l$ describes the variation along a spheroidal surface (for example, the plasma boundary) in a direction perpendicular to $\hat{\phi}$. In this paper, Secs. III and IV give a simple, detailed discussion of some of the $l=2$ modes and Sec. V gives a general discussion of higher-order modes of a Penning-trap plasma. Excitation of an $l=2$ mode produces a quadrupole deformation of the plasma shape. The $l=1$ modes are the familiar center-of-mass modes. Here the ion plasma's shape remains unchanged, but the center-of-mass of the plasma executes one of the three motions of a single ion in a Penning trap. For example, the (1,0) mode is the axial center-of-mass mode at frequency $\omega_z$. There are two (1,1) modes which correspond to the perturbed cyclotron and magnetron center-of-mass modes at frequencies $\Omega-\omega_m$ and $\omega_m$. (In experiments on long columns of electrons where the induced image charges cannot be neglected, the analog of the magnetron center-of-mass mode is the $l=1$ diocotron mode [37,38].) These center-of-mass frequencies can, in general, be measured or calculated very precisely. Figure 3 gives the (1,0) mode frequency or $\omega_z$ in units of the plasma frequency as a function of the plasma aspect ratio or shape. Because $\omega_p$ is typically unknown, a measurement of $\omega_z$ does not provide information on the plasma aspect ratio. However, measurement of an $l=2$ mode frequency along with the (1,0) mode frequency will determine the plasma's aspect ratio and density.

## III. QUADRUPOLE PLASMA MODES

In this section we calculate two different types of $l=2$ Penning-trap plasma modes. This is done by making a guess for the plasma eigenmode, then verifying that this guess is a mode of the plasma and calculating the eigenfrequency. In particular, we consider small axial and radial displacements of the ions from their equilibrium positions consistent with the assumed eigenmode. A self-consistent calculation of the axial and radial restoring forces gives two linear differential equations describing the motion of the axial and radial displacements. We then require that the eigenfrequencies from these two equations be equal.

### A. (2,0) modes

We first consider an azimuthally symmetric quadrupole mode. We assume that in this mode the plasma always stays spheroidal, but the aspect ratio of the plasma oscillates in time as shown in Fig. 5. This mode turns out to be a (2,0) mode [29]. Let $\tilde{\rho}\equiv x+iy$ and $z$ denote the equilibrium radial and axial position of an ion (or group of ions) in a plasma with an equilibrium density $n_0$ and aspect ratio $\alpha$. The displacements from equilibrium

$$\begin{aligned} z &\rightarrow z[1+\epsilon(t)] , \\ \tilde{\rho} &\rightarrow \tilde{\rho}[1+\tilde{\delta}(t)] , \end{aligned} \tag{3.1}$$

parametrized by $\epsilon$ and $\tilde{\delta}\equiv\delta_R+i\delta_I$, give another spheroidal plasma but with a density and aspect ratio given by

$$\begin{aligned} n_0 &\rightarrow \frac{n_0}{(1+\epsilon)|1+\tilde{\delta}|^2} , \\ \alpha &\rightarrow \alpha\frac{1+\epsilon}{|1+\tilde{\delta}|} , \end{aligned} \tag{3.2}$$

where $|1+\tilde{\delta}|=[(1+\delta_R)^2+\delta_I^2]^{1/2}$. Here $\epsilon$, $\delta_R$, and $\delta_I$ characterize axial, radial, and azimuthal displacements. For an eigenmode the axial and radial displacements should have the same time dependence. We assume

$$\frac{\epsilon(t)}{\delta_R(t)}=\eta , \tag{3.3}$$

where $\eta$, the mode parameter, is independent of time.

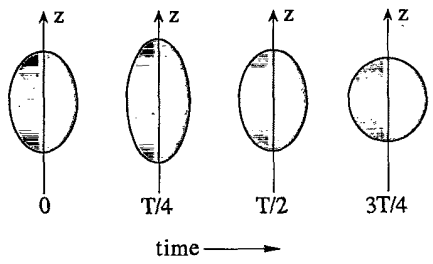


FIG. 5. Sketch of one cycle of the (2,0) mode at time intervals $T/4$ where $T=2\pi/\omega_{20}$ is the period of the mode. The plasma always stays spheroidal with a uniform density, but the aspect ratio oscillates in time.

Equations (2.4) and (2.9) can be used to calculate the electric field at the displaced ion positions with the results that

$$\begin{aligned} \tilde{E}_\perp &= \frac{m\omega_p^2}{3q}\left[\frac{3\omega_z^2}{2\omega_p^2}+\frac{a[\alpha(1+\epsilon)|1+\tilde{\delta}|^{-1}]}{(1+\epsilon)|1+\tilde{\delta}|^2}\right]\tilde{\rho}(1+\tilde{\delta}) \\ &\equiv \frac{m\omega_p^2}{3q}A(\tilde{\delta},\epsilon)\tilde{\rho}(1+\tilde{\delta}) , \end{aligned} \tag{3.4}$$

$$\begin{aligned} E_z &= \frac{m\omega_p^2}{3q}\left[-\frac{3\omega_z^2}{\omega_p^2}+\frac{b[\alpha(1+\epsilon)|1+\tilde{\delta}|^{-1}]}{(1+\epsilon)|1+\tilde{\delta}|^2}\right]z(1+\epsilon) \\ &\equiv \frac{m\omega_p^2}{3q}B(\tilde{\delta},\epsilon)z(1+\epsilon) . \end{aligned} \tag{3.5}$$

Here $\tilde{E}_\perp$ and $E_z$ are the components of the electric field perpendicular and parallel to the $z$ axis and $\omega_p$ is the equilibrium plasma frequency. The equations describing the radial and axial motions of the displaced ions are

$$\frac{d^2}{dt^2}\{\tilde{\rho}(1+\tilde{\delta})\}+i\Omega\frac{d}{dt}\{\tilde{\rho}(1+\tilde{\delta})\} - \frac{\omega_p^2}{3}A(\tilde{\delta},\epsilon)\tilde{\rho}(1+\tilde{\delta})=0 , \tag{3.6}$$

$$\frac{d^2}{dt^2}\{z(1+\epsilon)\}-\frac{\omega_p^2}{3}B(\tilde{\delta},\epsilon)z(1+\epsilon)=0 . \tag{3.7}$$

After transforming to a frame rotating at the equilibrium rotation frequency $\omega_r$ and keeping terms no higher than first order in $\tilde{\delta}$ and $\epsilon$, we obtain linear differential equations for $\tilde{\delta}$ and $\epsilon$. The equations are

$$\frac{d^2}{dt^2}\tilde{\delta}+i(\Omega-2\omega_r)\frac{d}{dt}\tilde{\delta}-\frac{\omega_p^2}{3}(\eta A_\epsilon+A_\delta)\delta_R=0 , \tag{3.8}$$

$$\frac{d^2}{dt^2}\epsilon-\frac{\omega_p^2}{3}\{B_\epsilon+B_\delta/\eta\}\epsilon=0 . \tag{3.9}$$

Here $A_\delta\equiv\partial A(0,0)/\partial\delta_R$ and $A_\epsilon\equiv\partial A(0,0)/\partial\epsilon$, with similar definitions for $B_\epsilon$ and $B_\delta$. There are no first-order $\delta_I$ terms in the expansion of $A$ and $B$, because $A$ and $B$ are even functions of $\delta_I$. The real and imaginary parts of Eq. (3.8) can be solved simultaneously. The solution is oscillatory with eigenfrequency $\omega_{20}$ given by

$$\omega_{20}^2=(\Omega-2\omega_r)^2-\frac{\omega_p^2}{3}(\eta A_\epsilon+A_\delta) . \tag{3.10}$$

The eigenfrequency of Eq. (3.9) is given by

$$\omega_{20}^2=\frac{-\omega_p^2}{3}\{B_\epsilon+B_\delta/\eta\} . \tag{3.11}$$

The requirement that the two eigenfrequencies be equal gives a quadratic equation for $\eta$. Substitution of the solutions for $\eta$ back into either Eq. (3.10) or (3.11) gives the (2,0) mode frequency $\omega_{20}$. After a number of algebraic manipulations we find

$$\left.\begin{matrix}2(\omega_{20}^{+})^2\\ 2(\omega_{20}^{-})^2\end{matrix}\right\}=\Omega_u^2+\omega_Q^2\left\{\begin{matrix}+\\ -\end{matrix}\right\}[(\Omega_u^2-\omega_Q^2)^2 -4\Omega_v^2(\omega_z^2-\omega_Q^2/3)]^{1/2}\ . \quad (3.12)$$

Here $\Omega_v\equiv\Omega-2\omega_r$ is the vortex frequency (the cyclotron frequency as seen in the rotating frame), $\Omega_u\equiv(\Omega_v^2+\omega_p^2)^{1/2}$ is the upper hybrid frequency, and

$$\omega_Q^2\equiv\omega_p^2\frac{3\alpha}{(\alpha^2-1)^{3/2}}Q_2^0\left[\frac{\alpha}{(\alpha^2-1)^{1/2}}\right]\ . \quad (3.13)$$

The lower-frequency mode [denoted by the negative sign in Eq. (3.12)] is called a plasma mode and is characterized by $\eta\leq 0$ and a mode frequency $\omega_{20}^{-}\leq\Omega/\sqrt{3}$. The higher-frequency mode [denoted by the positive sign in Eq. (3.12)] is called an upper hybrid mode and is characterized by $\eta\geq 0$ and a mode frequency $\omega_{20}^{+}\geq\Omega/\sqrt{3}$. Plasma and upper hybrid modes are discussed in Sec. V. The frequency $\omega_Q$ is the (2,0) plasma mode frequency in the absence of a magnetic field (that is, $\Omega_v\to 0$ or a plasma confined by a uniform background of opposite charge). It is a mode frequency of a cold cloud of ions in an rf trap.

Most Penning-trap experiments are done with $\omega_z\ll\Omega$. For simplicity we therefore discuss the two modes of Eq. (3.12) for this experimentally interesting case. Figure 6 shows a graph of $\omega_{20}^{+}$ and $\omega_{20}^{-}$ as a function of rotation frequency for $\omega_z/\Omega=0.151$. In the limit of low rotation frequencies ($\omega_r\to\omega_m$) the plasma mode frequency approaches $\omega_p$. At $\omega_r=\omega_m$, the mode frequency $\omega_{20}^{-}=\omega_p=\omega_z$. In this limit the mode parameter $\eta$ for the plasma mode frequency is large in magnitude and negative. The plasma mode looks predominantly like an axial stretch mode with only small radial excursions which are 180° out of phase with the axial excursions. This is because for $\omega_r\simeq\omega_m\ll\Omega$ the magnetic field in the rotating frame ($\propto\Omega-2\omega_r$) is large and constrains the radial excursions of the plasma. At the Brillouin limit ($\Omega_v=0$) or in a cold plasma confined in an rf trap, the plasma mode frequency equals $\omega_Q$ and the mode parameter $\eta=-2$. This means the volume and therefore the density of the plasma stay constant during the excitation of this mode. At the Brillouin limit, the plasma mode therefore consists of incompressible deformations of the plasma shape (a surface mode). The (2,0) plasma mode of a spheroidal plasma is similar to an $m=0$ plasma mode of a cylindrical plasma column with a wavelength equal to the plasma length [37,38].

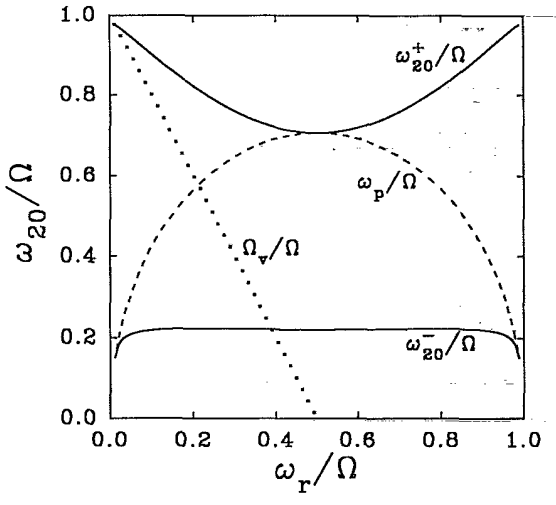


FIG. 6. Graph of the plasma $\omega_{20}^{-}$ and upper hybrid $\omega_{20}^{+}$ mode frequencies [from Eq. (3.12)] as a function of rotation frequency $\omega_r$ for $\omega_z/\Omega=0.151$. Also shown are the vortex frequency $\Omega_v=\Omega-2\omega_r$ (dotted line) and the plasma frequency $\omega_p$ (dashed line) in units of the cyclotron frequency.

The upper hybrid mode frequency approaches $\Omega_v=\Omega-2\omega_r$ for low rotation frequencies and is equal to $\Omega-2\omega_m$ at $\omega_r=\omega_m$. In this limit the mode parameter $\eta$ for the upper hybrid mode is small and positive (radial excursions $\gg$ axial excursions). For low rotation frequencies we can show that this mode looks like a coherent excitation of the perturbed cyclotron orbits of the ions. For two ions on opposite sides of the trap axis, the perturbed cyclotron orbits are 180° out of phase. At the Brillouin limit (or for ions confined in an rf trap), the upper hybrid mode is equal to $\omega_p=\Omega/\sqrt{2}$. Here $\eta=\alpha^{-2}$, which implies that the plasma oscillates (or "breathes") from a small spheroid to a larger confocal spheroid and back again. The electric field outside the plasma does not change under such an oscillation. This can be called a bulk mode because it is confined to the plasma interior and is difficult to couple to with external fields. Both of the (2,0) modes are symmetric (even functions) about the Brillouin condition ($\omega_r=\Omega/2$), as can be seen in Fig. 6.

If either one of the (2,0) mode frequencies can be measured, it can be used together with the (1,0) mode frequency $\omega_z$ and the cyclotron frequency $\Omega$ to obtain the plasma rotation frequency $\omega_r$. The plasma rotation frequency can then be used to determine the plasma's density $n_0$ and aspect ratio $\alpha$ from Eqs. (2.1), (2.2), and (2.6). Figure 7(a) shows points of constant $\omega_{20}^{+}$ (the upper hybrid frequency) and Fig. 7(b) shows points of constant $\omega_{20}^{-}$ (the plasma mode frequency) on graphs of rotation frequency versus the trap axial frequency. All frequencies are normalized by $\Omega$. The axial frequency $\omega_z$ [equivalently the (1,0) mode frequency] depends only on the trap design and the potential difference between the trap end cap and ring electrodes. Typically it can be measured or calculated very precisely. Similarly the cyclotron frequency can be measured or calculated very precisely and the operating point for $\omega_z/\Omega$ along the $x$ axis of Fig. 7 precisely determined. A measurement of a (2,0) mode frequency can then be used with Fig. 7 to determine the rotation frequency. Figure 7(b) shows that the plasma mode frequency $\omega_{20}^{-}$ gives accurate information on $\omega_r/\Omega$ mainly for slow rotation frequencies slightly greater than $\omega_m$. However, the upper hybrid frequency gives accurate information on $\omega_r/\Omega$ over a wide range of conditions, especially over the experimentally interesting range $\omega_z/\Omega\ll 1$. Section IV describes some (2,0) mode mea-

surements on plasmas of $^9Be^+$ ions. The modes were excited by applying an oscillatory potential between the ring electrode and the trap end caps which was resonant with the mode frequencies.

Figure 7 assumes a spheroidal plasma with $\lambda_D$, $n_0^{-1/3} \ll$ (plasma dimensions) as discussed in Sec. II. However, even for finite temperatures, the (2,0) modes should provide useful information on the plasma rotation frequency. For example, in the limit that the ion space-charge fields can be neglected, the upper hybrid mode frequency is $\Omega - 2\omega_m$. The difference between $\Omega - 2\omega_m$ and the measured upper hybrid mode frequency is therefore a measure of the importance of the space-charge fields. Also, an oscillatory drive on the ring electrode at $\Omega - 2\omega_m$ can parametrically excite the perturbed cyclotron motion of the plasma center of mass [the high-frequency (1,1) mode] whose frequency is $\Omega - \omega_m$ in the laboratory frame. This parametric excitation requires an initial, nonzero mode amplitude.

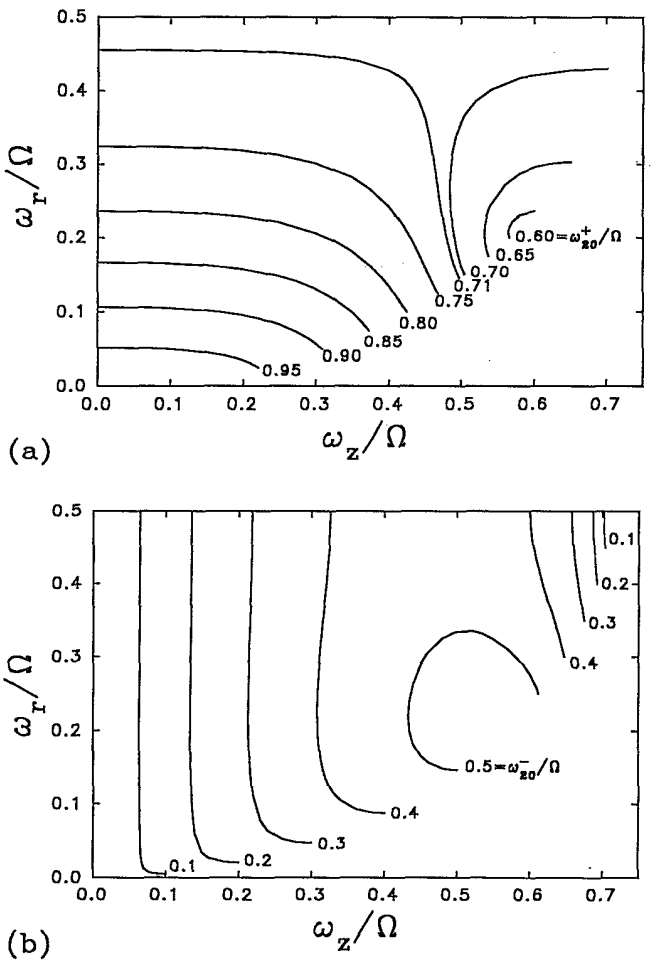


FIG. 7. Sensitivity of the (2,0) mode frequencies for determining the plasma rotation frequency. Points of constant (a) upper hybrid frequency $\omega_{20}^+$ or (b) plasma mode frequency $\omega_{20}^-$ are plotted on a graph of rotation frequency $\omega_r$ vs the trap axial frequency $\omega_z$ (in units of the cyclotron frequency $\Omega$). A measurement of $\omega_z$, $\Omega$, and $\omega_{20}^+$ or $\omega_{20}^-$ can be used with these graphs to determine the rotation frequency. The $\omega_{20}$ plots are symmetric about $\omega_r/\Omega = 0.5$. The boundary defined by the low-$\omega_r$ end of the curves denotes the condition $\omega_r = \omega_m$. Ion confinement requires $\omega_r \geq \omega_m$.

### B. (2,1) modes

We now consider an azimuthally asymmetric quadrupole mode. As in the previous section, we let $\tilde{\rho} \equiv x + iy$ and $z$ denote the equilibrium radial and axial position of an ion (or group of ions) in a plasma with an equilibrium density $n_0$ and aspect ratio $\alpha$. We guess that there is a mode described by displacements from equilibrium of the form

$$\begin{aligned} x &\to x + \delta z \cos(\omega_{21}^{\text{lab}} t) , \\ y &\to y + \delta z \sin(\omega_{21}^{\text{lab}} t) , \\ z &\to z + \epsilon[x \cos(\omega_{21}^{\text{lab}} t) + y \sin(\omega_{21}^{\text{lab}} t)] . \end{aligned} \tag{3.14}$$

As the subscripts in Eq. (3.14) indicate, this turns out to be a (2,1) mode. The superscript lab indicates that the description is in the laboratory frame of reference. [This labeling was not required with the azimuthally symmetric (2,0) mode because its frequency is the same in either the laboratory or rotating frame.] Equation (3.14) can be rewritten using complex notation as

$$\begin{aligned} \tilde{\rho} &\to \tilde{\rho} + \tilde{\delta}(t) z , \\ z &\to z + \mathrm{Re}\{\tilde{\epsilon}(t) \tilde{\rho}^*\} , \end{aligned} \tag{3.15}$$

where the time dependence is now included in $\tilde{\delta}(t)$ and $\tilde{\epsilon}(t)$, the asterisk denotes the complex conjugate, Re denotes the real part, and

$$\frac{\tilde{\epsilon}(t)}{\tilde{\delta}(t)} = \eta , \tag{3.16}$$

where the mode parameter $\eta$ is independent of time and real. Equation (3.15) transforms a uniform density spheroid into a uniform density ellipsoid. The ellipsoid is rotated with respect to the original, equilibrium spheroid by an angle $|\tilde{\gamma}|$, where, to first order in $\tilde{\epsilon}$ and $\tilde{\delta}$,

$$\tilde{\gamma} = \frac{\tilde{\delta}\alpha^2 + \tilde{\epsilon}}{1 - \alpha^2} . \tag{3.17}$$

The modulus $|\tilde{\gamma}|$ denotes the magnitude of the rotation angle. The phase of $\tilde{\gamma}$ denotes the plane in which the rotation takes place. Specifically, the rotation occurs about the unit vector ( $\mathrm{Im}\tilde{\gamma}/|\tilde{\gamma}|$, $-\mathrm{Re}\tilde{\gamma}/|\tilde{\gamma}|$,0) or, equivalently, the $\tilde{\rho} = -i\tilde{\gamma}$ axis. To first order in $\tilde{\epsilon}$ and $\tilde{\delta}$, the tilted ellipsoid is a spheroid with the same aspect ratio as the equilibrium spheroid. Therefore to calculate the electric field at the displaced ion positions to first order in $\tilde{\epsilon}$ and $\tilde{\delta}$, we have only to calculate the electric field inside the equilibrium spheroid rotated by an angle $|\tilde{\gamma}|$ about the $\tilde{\rho} = -i\tilde{\gamma}$ axis. We obtain

$$\tilde{E}_\perp \simeq \frac{m\omega_p^2}{2q}(\tilde{\rho} + \tilde{\delta} z) + \frac{m\omega_p^2}{3q}(a - b)\tilde{\gamma} z , \tag{3.18}$$

$$E_z \simeq \frac{m\omega_p^2}{2q}(a - b)\,\mathrm{Re}\{\tilde{\gamma}\tilde{\rho}^*\} . \tag{3.19}$$

Here $\omega_p$ is the equilibrium plasma frequency and $a(\alpha)$ and $b(\alpha)$ are evaluated at the equilibrium aspect ratio $\alpha$.

After transforming to a frame rotating at the equilibrium rotation frequency, the following differential equations are obtained for $\tilde{\delta}_r \equiv \exp\{i\omega_r t\}\tilde{\delta}$ and $\tilde{\varepsilon}_r \equiv \exp\{i\omega_r t\}\tilde{\varepsilon}$:

$$\frac{d^2}{dt^2}\tilde{\delta}_r + i\Omega_v \frac{d}{dt}\tilde{\delta}_r - \frac{\omega_p^2}{3} f(\alpha)(\alpha^2+\eta)\tilde{\delta}_r = 0 , \tag{3.20}$$

$$\frac{d^2}{dt^2}\tilde{\varepsilon}_r - \frac{\omega_p^2}{3} f(\alpha)\left[\frac{\alpha^2}{\eta}+1\right]\tilde{\varepsilon}_r = 0 . \tag{3.21}$$

Here $f(\alpha) \equiv [a(\alpha)-b(\alpha)]/(1-\alpha^2) = \frac{3}{2}(1-3\omega_z^2/\omega_p^2)/(1-\alpha^2)$. With the convention that the time dependence of $\tilde{\delta}_r$ and $\tilde{\varepsilon}_r$ is given by $\exp(i\omega_{21}t)$, Eqs. (3.20) and (3.21) give the following two equations for $\omega_{21}$, the (2,1) mode eigenfrequency in the rotating frame. We obtain

$$-\omega_{21}^2 - \Omega_v\omega_{21} - \frac{\omega_p^2}{3} f(\alpha)(\alpha^2+\eta) = 0 , \tag{3.22}$$

$$-\omega_{21}^2 - \frac{\omega_p^2}{3} f(\alpha)\left[\frac{\alpha^2}{\eta}+1\right] = 0 . \tag{3.23}$$

When Eqs. (3.22) and (3.23) are solved simultaneously, a cubic equation for $\eta$ is obtained,

$$\Omega_v^2\eta + \frac{\omega_p^2}{3} f(\alpha)(\alpha^2+\eta)(\eta-1)^2 = 0 . \tag{3.24}$$

Solutions for $\eta$ from Eq. (3.24) can be plugged back into either Eq. (3.22) or (3.23) to obtain values of $\omega_{21}$ for three different (2,1) modes. The laboratory (2,1) mode frequency $\omega_{21}^{\rm lab}$ is obtained from $\omega_{21}^{\rm lab} = \omega_{21} - \omega_r$. With the convention used here, a positive $\omega_{21}$ ($\omega_{21}^{\rm lab}$) denotes a counterclockwise precession when viewed from above the $x$-$y$ plane in the rotating (laboratory) frame. This agrees with the usual right-hand rule for the sign of an angular frequency.

Figure 8 shows a graph of the three different (2,1) mode frequencies (in the laboratory) versus rotation frequency for $\omega_z/\Omega = 0.151$. As discussed in the previous two paragraphs, all three modes correspond to a tilt of the equilibrium spheroid with respect to the $z$ axis. This tilted spheroid then precesses about the trap symmetry axis at the frequency $\omega_{21}^{\rm lab}$ as shown in Fig. 9. Because the density remains constant during the mode excitation, all three (2,1) modes are surface modes. The modes with the highest and lowest values of $|\omega_{21}^{\rm lab}|$ are characterized by $\eta \geq 0$ (axial and radial excursions in phase). The third mode with intermediate frequency is characterized by $\eta \leq 0$ (axial and radial excursions 180° out of phase). For the mode with the highest value of $|\omega_{21}^{\rm lab}|$ in Fig. 8, the tilted spheroid precesses rapidly at a frequency near $\Omega$. For $\omega_r \simeq \omega_m \ll \Omega$, the mode frequency approaches $\omega_{21}^{\rm lab} \simeq -(\Omega-\omega_r)$ and the mode parameter satisfies $\eta \ll 1$. Equations (3.15) and (3.16) show that the axial excursions are small compared to the radial excursions and the precession can be thought of as being due to a coherent (although asymmetric in $z$) excitation of individual ion cyclotron orbits. For low rotation frequencies, this mode is classified as an upper hybrid mode (see Sec. V). For the mode with the lowest $|\omega_{21}^{\rm lab}|$ in Fig. 8, the tilted spheroid precesses at a low frequency. For $\omega_z \ll \Omega$ and $\omega_r \simeq \omega_m \ll \Omega$, the mode parameter satisfies $\eta \gg 1$ and $\omega_{21}^{\rm lab} \simeq \omega_z - \omega_r$. Here this mode can be thought of as a coherent (and azimuthally asymmetric) excitation of the axial motion of individual ions. For low rotation frequencies, this mode is classified as a magnetized plasma mode (see Sec. V). At the Brillouin limit, the highest- and lowest-frequency modes both have $\eta = 1$, and their frequencies are equally spaced about $-\Omega/2$. Stated

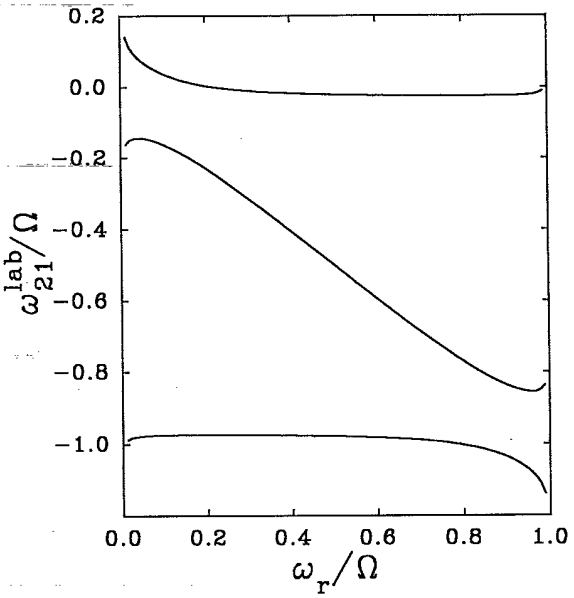


FIG. 8. Graph of the three (2,1) mode frequencies $\omega_{21}^{\rm lab}$ as a function of the plasma rotation frequency $\omega_r$ for $\omega_z/\Omega = 0.151$. The mode frequencies in the laboratory frame are plotted. The mode with the lowest value of $|\omega_{21}^{\rm lab}|$ has a frequency equal to 0 for $\omega_r/\Omega = 0.219$.

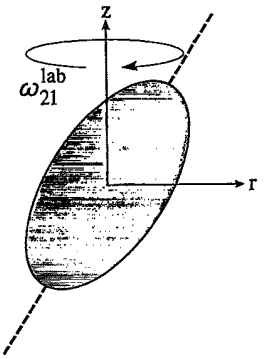


FIG. 9. Sketch of the (2,1) mode in the laboratory frame. The plasma spheroid is tilted with respect to the $z$ axis and precesses about the $z$ axis at $\omega_{21}^{\rm lab}$. In this figure the sense of the precession is positive. The picture in the rotating frame is the same except the precession occurs at the frequency $\omega_{21} = \omega_{21}^{\rm lab} + \omega_r$.

differently, in the rotating frame the two modes have equal and opposite frequencies at the Brillouin limit. Near the Brillouin limit, these two modes are classified as evanescent modes (see Sec. V). The intermediate frequency mode has $\eta<0$. For $\omega_z \ll \Omega$ and $\omega_r \simeq \omega_m \ll \Omega$, the intermediate mode has $|\eta| \gg 1$ and $\omega_{21}^{\text{lab}} \simeq -\omega_z - \omega_r$. Therefore this mode has an interpretation similar to the lowest-frequency mode. However, the behavior of this mode is quite different for $\omega_r \gg \omega_m$. At the Brillouin limit $\eta=-\alpha^2$, which means that the plasma shape does not change (that is, the plasma spheroid does not tilt), and this mode frequency in the rotating frame is 0. Therefore this mode vanishes at the Brillouin limit and is called a magnetized plasma mode (see Sec. V).

Figure 8 shows that the (2,1) mode with the lowest magnitude of frequency in the laboratory frame is 0 at $\omega_r/\Omega=0.219$ for $\omega_z/\Omega=0.151$. This zero-frequency mode can be excited by a static field error [19,21,39]. From the ion's point of view (the rotating frame) the static field error looks like a rotating field with a frequency $\omega_r$. When $\omega_{21}=\omega_r$ or $\omega_{21}^{\text{lab}}=\omega_{21}-\omega_r=0$ the (2,1) mode is excited. Section IV describes the excitation of the static (2,1) mode by a tilt of the electrode symmetry axis of the trap relative to the trap magnetic field axis. If the rotation frequency $\omega_r$ was increased from small values by an external torque, excitation of this mode tended to limit $\omega_r$ to values less than the rotation frequency where $\omega_{21}^{\text{lab}}=0$.

In addition to the (2,0) and (2,1) modes, there are two (2,2) modes. The (2,2) modes are discussed with the other $l=m$ modes in Sec. V. In a (2,2) mode, the plasma forms an ellipsoid with unequal principal axes in the $x$-$y$ plane. The ellipsoid rotates about the $z$ axis at the (2,2) mode frequency. A measurement of one of the (2,1) or (2,2) mode frequencies can be used to determine the plasma rotation frequency and aspect ratio in the same manner as described for the (2,0) modes (see Fig. 7).

## IV. EXPERIMENTAL RESULTS

In this section we compare experimental measurements of some quadrupole modes of a Penning-trap plasma with the calculations of Sec. III. Much of the experimental work has been described previously in Ref. [21]. Typically between 1000 and 5000 $^9Be^+$ ions were stored in a cylindrical Penning trap shown schematically in Fig. 1. Most of the experimental work was done with $B=0.82$ T where $\Omega(^9Be^+)/2\pi=1400$ kHz. Some singly charged, heavier ions were created when the $^9Be^+$ ions were created or loaded into the trap. In addition, singly charged, heavier ions slowly formed after loading $^9Be^+$, presumably due to ion-molecule reactions involving the $^9Be^+$ ions. Their presence appeared to shift the observed mode frequencies. We could eliminate them from the trap by momentarily raising $V_T$ so that $\omega_z/\Omega>1/\sqrt{2}$ for the heavier ions, making them unstable. In practice we would raise $V_T$ to satisfy $\omega_z/\Omega\simeq 0.67$ for $^9Be^+$. We then obtained repeatable and consistent measurements for the mode frequencies.

Radiation pressure from a laser was used to cool the $^9Be^+$ plasma [20,21,28]. A 313-nm laser (power $\simeq 100\ \mu$W) was tuned 10–50 MHz below the rest frequency $\omega_0$ of the $2s\,^2S_{1/2}(m_I=+\frac{3}{2},\ m_J=+\frac{1}{2}) \rightarrow 2p\,^2P_{3/2}(\frac{3}{2},\frac{3}{2})$ transition in $^9Be^+$. In addition to cooling the ions, this laser optically pumped the ions into the $(\frac{3}{2},\frac{1}{2})$ ground state [28]. The ions were detected by imaging the laser-induced ion fluorescence onto the photocathode of a photon-counting imaging tube (see Fig. 1). A real-time display of the image was used to monitor qualitatively the plasma's kinetic energy; a hot plasma had a more diffuse boundary and less ion fluorescence. With this simple diagnostic we were unable to distinguish between an increase in the random thermal energy of the ions and the excitation of a coherent modal motion of the plasma. The cooling laser was split into two beams. One beam (shown in Fig. 1) was directed perpendicularly to the $z$ axis near the center of the trap. The second beam (not shown in Fig. 1) was used along with the first beam when the lowest ion temperatures were desired [20,21,28]. It was directed at a 51° angle with respect to the $z$ axis. (The projection of this beam along the $z$ axis cooled the ion's axial motion directly.) With laser cooling, the $^9Be^+$ ions quickly evolved into a near thermal equilibrium distribution and could be confined for many hours [28]. The temperature of the ions could be measured from the Doppler broadening of an optical transition [28]. Typical temperatures ranged from 5 to 200 mK. (Here temperature refers to the Maxwell-Boltzmann velocity distribution which occurs in thermal equilibrium in the rotating frame.)

The plasma density was determined from Eq. (2.1) by measuring the plasma rotation frequency. We measured the rotation frequency by driving the $(m_I=+\frac{3}{2},\ m_J=+\frac{1}{2}) \rightarrow (+\frac{3}{2},-\frac{1}{2})$ electron spin-flip transition at frequency $\omega_s$ in the $2s\,^2S_{1/2}$ $^9Be^+$ ground state. The transition frequency $\omega_s$ is approximately equal to 22 GHz at $B=0.82$ T. The transition was observed as a decrease in the ion fluorescence when the frequency of the applied microwave field is resonant with $\omega_s$ [40]. In addition, a decrease in the ion fluorescence was observed at the sideband frequencies $\omega_s\pm\omega_r$. This is because from the ion's point of view the phase and amplitude of the microwave field are modulated due to the rotation of the plasma. This produces sidebands in the microwave spectrum observed by the ions at $\omega_s\pm\omega_r$ [41]. Measurement of these sidebands enabled $\omega_r/2\pi$ to be determined to about 5 kHz. At $B=0.82$ T, the $^9Be^+$ ion densities usually were measured to be greater than $10^7/cm^3$. This density with temperatures less than 200 mK results in Debye lengths less than 10 $\mu$m. With 1000–5000 ions in the trap, the typical plasma dimensions were between 100 and 1000 $\mu$m, which is one or two orders of magnitude larger than $\lambda_D$. The radius of the cylindrical trap electrodes (1.27 cm) was another order of magnitude larger. Consequently the laser-cooled $^9Be^+$ plasmas satisfied the condition $\lambda_D \ll$(plasma dimensions)$\ll$(trap dimensions) and formed constant density, spheroidal plasmas. The axial frequency $\omega_z$ was measured by applying an oscillating potential to one of the end caps [42]. The cyclotron frequency $\Omega$ was calculated from the magnetic field. The magnetic field was determined accurately from measure-

ments of the electron spin-flip or nuclear spin-flip transition frequencies in the $^9Be^+$ ground state.

The angular momentum and therefore the rotation frequency $\omega_r$ of the $^9Be^+$ plasmas were controlled by a torque from the radiation pressure of a second, weak laser beam (power $\simeq 2$ $\mu$W) whose frequency $\omega_T$ was tuned above the cooling transition frequency $\omega_0$. This torque beam (see Fig. 1) was directed perpendicularly to the $z$ axis but displaced from the $z$ axis through the side of the plasma which recedes from the laser beam due to the plasma rotation. This beam imparted to the plasma a torque which tended to increase the plasma rotation frequency $\omega_r$. Initially the plasma was cooled by the cooling laser beam with the result that $\omega_r \ll \Omega$. The torque laser beam was then directed through the side of the plasma with a frequency $\omega_T$ tuned slightly below $\omega_0$. As $\omega_T$ was increased above $\omega_0$, $\omega_T$ became resonant with the frequency of the Doppler-shifted ions in the torque beam. This produced ion fluorescence and a torque on the plasma which increased the rotation frequency. As shown in Fig. 4, an increase in $\omega_r$ produced a decrease in the plasma radius $r_0$ for $\omega_r < \Omega/2$ and an increase in $r_0$ for $\omega_r > \Omega/2$. The plasma radius was measured with the imaging tube. Accurate measurements of the plasma's axial extent were more difficult to obtain. However, we could qualitatively check that the plasma obtained its maximum axial extent (and therefore maximum aspect ratio) at the Brillouin limit by scanning the position of one of the laser beams along the axial direction.

By appropriate tuning of the torque laser frequency and with some adjustment of the positions of the cooling and torque lasers, we could obtain a steady-state, equilibrium plasma with a rotation frequency anywhere in the allowed range from $\omega_m$ to $\Omega - \omega_m$. In addition to supplying a torque, the torque laser also supplied energy to the plasma when $\omega_T > \omega_0$ [43]. Equilibrium occurred when the energy input from the torque laser was removed by the cooling laser and when the laser beam torques and torques from static field asymmetries summed to 0. We were also able to increase $\omega_r$ to values greater than $\Omega/2$ by using just the cooling laser. An increase in the cooling laser frequency increased $\omega_r$. In this case, however, the rotation frequency sensitively depended on the cooling laser frequency and a steady-state condition was more difficult to achieve.

We discovered [21] that as the plasma rotation frequency was increased, there was a range of rotation frequencies where the plasma acquired a diffuse boundary and a low level of ion fluorescence characteristic of a hot plasma. The range over which this apparent heating occurred depended sensitively on the alignment of the trap's symmetry axis with the magnetic field axis. Let $\theta_0$ denote the angle between these two axes. If we assume that the trap is aligned when the apparent heating resonance is minimized, then we could adjust $\theta_0 < 0.01°$ by searching for an alignment which gave no apparent heating. For $\theta_0 > 0.1°$ the plasma rotation frequency could not be increased beyond the point at which heating first occurred. This heating resonance appeared to get stronger with an increase in the number of ions. We have been able to identify this heating resonance as an excitation of a collective (2,1) plasma mode by the static field asymmetry associated with the misalignment of the trap symmetry axis with the magnetic field. Figure 10 shows the measured rotation frequencies where heating occurred with $\theta_0 \simeq 0.02°$ for different trap axial frequencies. Also shown (solid line) is the calculated rotation frequency at which $\omega_{21}^{\rm lab} = 0$, that is, $\omega_r = \omega_{21}$ as calculated from Eqs. (3.22)–(3.24). Excellent agreement is obtained between the predicted and measured rotation frequencies where heating is observed.

We did not attempt to understand the source of energy in the heating resonance. However, two possibilities are listed below. A static asymmetry cannot change the total energy of the plasma, but it can convert potential to thermal energy by producing an expansion of the plasma. Because the ratio of potential to thermal energy is large in our plasmas, a small expansion can produce a large increase in the ion thermal energy. This energy source increases with the potential energy per ion of the plasma. For example, it increases with the ion number or plasma density. With the lasers operating continuously, the time-averaged plasma radius does not change. However, the plasma radius may fluctuate. For example, there could be a small plasma expansion between photon scattering events, balanced by a plasma contraction when a photon is scattered. Heat could be generated by expansion during plasma fluctuations. Another source of energy is the torque laser. The energy input from this laser could increase when the static (2,1) resonance is excited if there is an increase in the scatter rate from this laser.

If the density is increased from low values corresponding to $\omega_r \ll \Omega/2$, excitation of the static (2,1) mode may provide a practical limit to the density and number of charged particles that can be stored in a Penning trap. For large ion numbers or $\theta_0 > 0.1°$ we were unable to obtain densities greater than $n_0(\omega_r = \omega_{21})$. For $\omega_z/\Omega > 0.53$, Fig. 10 shows that $\omega_r = \omega_{21}$ occurs for

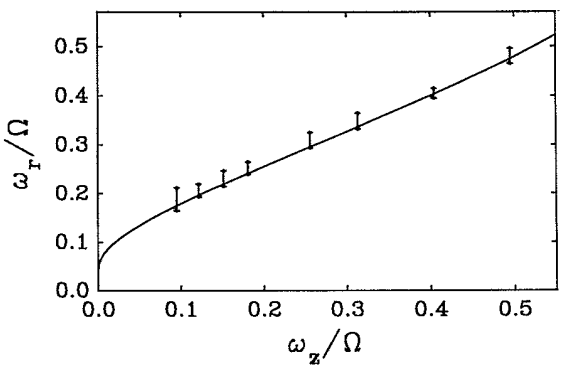


FIG. 10. Rotation frequency $\omega_r$ at which heating was observed as a function of the single-particle axial frequency $\omega_z$. Both frequencies are expressed in units of the cyclotron frequency $\Omega$. The experimental data were obtained with 1000–5000 $^9Be^+$ ions stored in the trap of Fig. 1. The solid line indicates the calculated rotation frequency $\omega_r$ at which $\omega_{21} = 0$. This is a universal curve involving no adjustable parameters.

$\omega_r/\Omega > 0.5$ and therefore the static (2,1) mode will not prevent reaching the Brillouin limit in this case. However, for a high magnetic field and a trap with large dimensions, the condition $\omega_z/\Omega > 0.53$ may be difficult to obtain because of practical limitations on the voltage that can be applied to the trap electrodes. In addition, $\omega_r/\Omega = 0.5$ with $\omega_z/\Omega = 0.53$ occurs for an aspect ratio $\alpha = 0.44$. For storage of a large number of charged particles, this would require a trap with a large radius. However, a large volume trap is more easily constructed by extending it axially while keeping the radius fixed [44]. For storage of large ion numbers, the plasma dimensions may not be small compared to the trap dimensions. This changes the calculation of the modes because the trap potential will not, in general, be quadratic and the image charges in the trap electrodes cannot be neglected. In spite of the difficulty of increasing $\omega_r$ (and the density) through the point where the heating resonance occurs, there is still the potential to "jump through" this condition by sudden switching of $\omega_z$ or creating the plasma with $\omega_r > |\omega_{21}|$.

Laser torques were also used to increase $\omega_r$ in $^9Be^+$ plasmas consisting of 40 000 $^9Be^+$ ions at $B = 6$ T. We were unable to remove possible contaminant ions at this high magnetic field because of the high voltages required on the trap electrodes. In addition, we did not have a microwave source ($\simeq 160$ GHz at $B = 6$ T) to drive the ground-state electron spin-flip transition and measure the plasma rotation frequency. However, a rough measure of $\omega_r$ could be obtained from the plasma aspect ratio. We were able to obtain rotation frequencies $\omega_r > \Omega/2$. Figure 11 shows an image of a rapidly rotating $Be^+$ plasma with $\omega_r/2\pi \simeq \Omega/2\pi = 10$ MHz. The propeller shape of the ion fluorescence is due to the fast rotation of the plasma. The ions get excited in the laser beam, but decay outside the laser beam because the 8.2-ns lifetime of the excited $P$ state is longer than the typical transit time through the beam. The (2,1) heating resonance was much stronger and more sensitive to the magnetic field alignment at $B = 6$ T than in our work at 0.8 T. This may have been due to the larger number of trapped ions at $B = 6$ T. We also observed additional heating resonances at lower rotation frequencies than the (2,1) heating resonance. Section V discusses other static modes that are potential candidates for these additional heating resonances. We note that many of these resonances tend to limit the plasma density to even lower values than the static (2,1) resonance.

FIG. 11. Image of the ion fluorescence of a rapidly rotating $^9Be^+$ plasma at $B = 6$ T with $\omega_r/2\pi \simeq \Omega/2\pi = 10$ MHz. Fluorescence due to the perpendicular and diagonal cooling beams is observed. The plasma diameter in the $z = 0$ plane is approximately 1 mm. The ion kinetic energy due to rotation at the radial edge of the plasma is approximately 50 eV.

Density limits on trapped ion plasmas have also been reported in other Penning-trap experiments. In Ref. [45] the experimentally observed ion fluorescence in a Penning trap was interpreted in terms of limits to the ion density imposed by single-particle resonant transport [46]. In single-particle resonant transport, enhanced transport (and lower ion density) may occur when the axial bounce frequency of an individual ion is commensurate with the ion's rotation frequency. In this process an individual ion resonantly interacts with an external field error. This is different from transport due to the excitation of a zero-frequency mode where a collective plasma mode resonantly interacts with an external field error. In our work we observe no evidence for single-particle resonant transport as an important mechanism for limiting the ion density. An important difference between our work and that of Ref. [45] is the ion temperature. In our work the ions are sufficiently cold that the ion-ion collision time is short compared to the axial bounce time. The experimental measurements of Ref. [45] were done on relatively hot ion clouds ($\simeq 5000$ K) where the ions may bounce faster than they collide. In addition, the Debye length in this work was likely comparable to or larger than the cloud dimensions. In this case the ion density is not constant, and calculation of the space-charge-shifted axial bounce frequency of an individual ion requires a model different from the cold thermal equilibrium discussed in Sec. II. The theoretical analysis of Ref. [45] would be more convincing with a self-consistent calculation of the space-charge shifts. Such a self-consistent calculation is described in Ref. [47]. When space charge is important, the potential variation in the axial direction is no longer harmonic, so the axial bounce frequency depends on the ion temperature and axial dimension of the ion cloud. Both of these dependencies are neglected in Ref. [45].

We also measured the (2,0) plasma and upper hybrid modes. These modes were excited by applying a sinusoidal potential between the two central and two outer electrodes in Fig. 1. They were detected by a change in the ion fluorescence when the frequency of the applied rf was resonant with the mode frequency. This change was presumably caused by a change in the ions' Doppler width and possibly by a change in the laser beam–plasma overlap. Measurements of the plasma mode frequency as a function of the plasma rotation frequency are shown in Fig. 12 for two different trap axial frequencies. The solid lines show the plasma mode frequency calculated from Eqs. (3.12), (3.13), and (2.6). Again, good agreement between the predicted and ob-

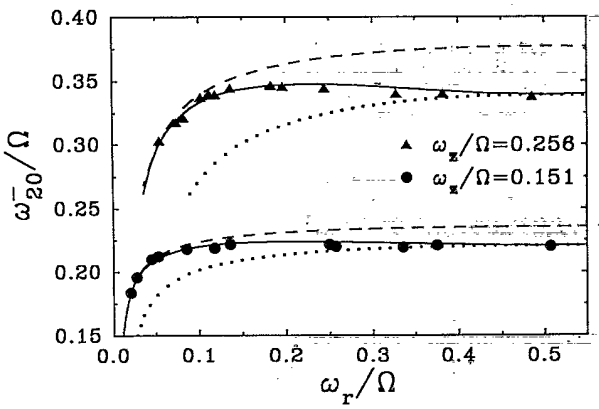


FIG. 12. Plasma mode frequency $\omega_{20}^{-}$ as a function of the rotation frequency $\omega_r$ for two different axial frequencies $\omega_z$. All frequencies are expressed in units of the cyclotron frequency $\Omega$. The circles and triangles give the experimental data. The solid lines give the cold-fluid model predictions for $\omega_{20}^{-}$. The dashed and dotted lines give the high- and low-magnetic-field calculations for $\omega_{20}$, respectively. The dotted line corresponds to the $\omega_{20}^{-}$ frequency for an rf-trap plasma with the same density and aspect ratio.

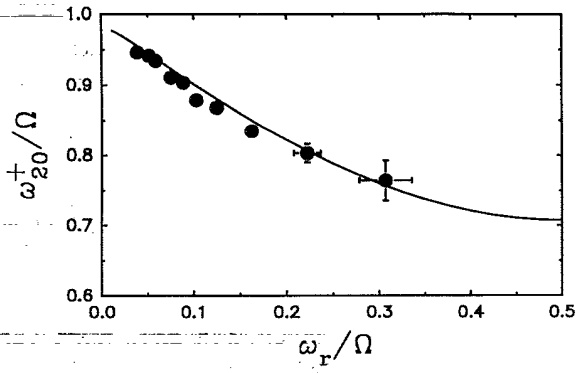


FIG. 13. Upper hybrid mode frequency $\omega_{20}^{+}$ as a function of the rotation frequency $\omega_r$ for $\omega_z/\Omega=0.151$. All frequencies are expressed in units of the cyclotron frequency $\Omega$. The circles give the experimental data. The uncertainty for measurements done at low rotation frequencies is approximately the size of the circles. At high rotation frequencies the uncertainties increase because the mode becomes difficult to excite. The solid line gives the cold-fluid model predictions.

served modes is obtained with no adjustable parameters. Figure 12 shows two additional calculations. In the first, shown as dashed lines, the magnetic field is assumed to be effectively infinite; that is, the ions are not allowed to move radially, and the mode frequency is calculated assuming a simple axial stretch of the charged spheroid. The mode frequency in this case is calculated from Eq. (3.11) by setting the $B_\delta/\eta$ term equal to 0. In the second calculation, shown as dotted lines, the magnetic field is assumed to be effectively 0; that is, the curve shows $\omega_Q$ [see Eq. (3.13)]. From this figure, the (2,0) plasma mode behaves like a mode of a strongly magnetized plasma at low rotation frequencies and an unmagnetized plasma near the Brillouin limit. We attempted to excite the upper hybrid (2,0) mode with a drive frequency near the upper hybrid frequency. A resonance (a change in the ion fluorescence) was observed as the frequency of the applied rf was swept. The amplitude of the drive was decreased until the resonance signal was barely detectable. Figure 13 shows a plot of the measured resonance frequency along with a calculation of the upper hybrid (2,0) mode from Eqs. (3.12), (3.13), and (2.6). Agreement is good, indicating that the observed resonance was likely the excitation of the upper hybrid (2,0) mode. As discussed in Sec. V, our drive could also potentially excite an upper hybrid (4,0) mode. For the conditions of this experiment, the two mode frequencies would be difficult to distinguish. However, for sufficiently weak drive strength, the (2,0) mode should be excited more strongly than the (4,0) mode. We could not excite this upper hybrid mode near the Brillouin limit because, as discussed in Secs. III and V, the upper hybrid modes become difficult to couple to with external fields there.

The agreement obtained here with the zero-temperature calculations requires that $\lambda_D \ll$(plasma dimensions) $\ll$(trap dimensions). This condition is usually easy to satisfy with a laser-cooled ion plasma and, in fact, may not be difficult to satisfy with a cryogenic ($T=4$ K) plasma. For example, a plasma with $n_0 \simeq 10^7/\text{cm}^3$ at $T=4$ K has a Debye length $\lambda_D=44$ $\mu$m. Consequently if the dimensions of this plasma are greater than 1 mm, the inequality $\lambda_D \ll$(plasma dimensions) is satisfied. A plasma with $z_0=r_0\simeq 1$ mm and $n_0\simeq 10^7/\text{cm}^3$ requires loading $4\pi r_0^3 n_0/3=4\times 10^4$ charged particles within 1 mm of the trap axis. The charged particles must then be cooled and evolve into a thermal equilibrium state before the plasma radius expands [18,46] due to radial transport produced by trap asymmetries. For electrons this appears to be possible because at large magnetic fields ($B\simeq 6$ T) the cyclotron radiation time is short ($<1$ s) and the time over which the plasma spreads due to trap asymmetries can be long [16] (many hours). In addition, localized sources such as field emission points can be used to load many electrons close to the trap axis. For ions which cannot be laser cooled the inequality for a zero-temperature plasma may be more difficult to achieve. This is because radiative cooling times are typically longer. In addition, the radial transport in Penning traps due to trap asymmetries is likely faster for ions than electrons because of the larger ion mass. However, with care in loading the plasma, or with the development of a technique to reduce the plasma radius and increase the ion density, it should be possible to satisfy the conditions for a zero-temperature plasma with ions at 4 K. Ions in a Paul trap can be rapidly cooled to the temperature of a background buffer gas. In this case it should be possible to obtain a plasma where the Debye length is small compared to the plasma dimensions. Some experiments in Paul traps approximate this regime [47].

## V. GENERAL LINEAR MODES

The quadratic oscillations discussed in Secs. III and IV are important special cases of an infinite set of linear nor-

mal modes. Although we have, up to now, emphasized the behavior of the quadratic modes, there are several reasons to consider the general modes here. First, although the general higher-order modes have not yet been experimentally measured, we will see that it should be possible to observe at least a few of them using the same experimental techniques as were described in Sec. IV. Second, a deeper understanding of the quadratic modes may follow from consideration of their place in the hierarchy of general oscillations. Finally, a simple exact analytic solution for all of these modes has been found [29].

In Sec. V A we briefly review some features of this general solution. We then discuss a simple form of the general dispersion relation for the modes which allows one to obtain numerical solutions of the mode frequencies using a polynomial-root-finding algorithm. We also consider some examples, including some of the modes which can be resonantly driven by applying an oscillating potential between the two end electrodes and the center electrodes. In Sec. V B, we focus on modes which can be resonantly driven by static field errors. We find that such resonances occur in profusion, becoming dense when the cloud rotation frequency is small compared to the cyclotron frequency.

### A. Description of the normal modes

In order to obtain a general solution for the normal modes several assumptions must be made. We assume the cloud is near thermal equilibrium, and we assume the oscillations around this equilibrium are small so that we can linearize the equations of motion. The temperature is assumed to be sufficiently small that pressure effects on the fluid dynamics are negligible, and correlation effects are also neglected; these are good approximations provided that both the Debye length and interparticle spacing are small compared to both the size of the cloud and the wavelength of the mode. Electromagnetic effects are neglected (that is, $\nabla\times\mathbf{E}=\nabla\times\mathbf{H}=0$ in Maxwell's equations) since the cloud is small and the mode frequency is relatively low, and the effect on the dynamics of image charges in the electrodes is neglected.

These approximations are identical to those used in the earlier sections and apply well to present experiments on small cold ion clouds. However, unlike in the previous analysis, we do not assume a particular form for the density perturbations. Rather, a general linear perturbation is employed. The dynamics are described in a frame rotating at the constant rotation frequency $\omega_r$ of the equilibrium plasma. In this frame the plasma is stationary and the density, fluid velocity, and the potential are perturbed from their equilibrium values:

$$n(\mathbf{x},t)=n_0(\mathbf{x})+\delta n(\mathbf{x},t)\ , \tag{5.1a}$$

$$\mathbf{v}(\mathbf{x},t)=0+\delta\mathbf{v}(\mathbf{x},t)\ , \tag{5.1b}$$

$$\phi(\mathbf{x},t)=\phi_0(\mathbf{x})+\psi(\mathbf{x},t)\ , \tag{5.1c}$$

where $\delta n$, $\delta\mathbf{v}$, and $\psi$ are the perturbed density, fluid velocity, and potential, respectively. The equilibrium density $n_0(\mathbf{x})$ is uniform within the plasma spheroid and zero outside, and $\phi_0$ is the total equilibrium potential in a rotating frame, equal to [28]

$$\phi_0=\phi_T+\phi_I+\frac{m\omega_r}{2q}(\Omega-\omega_r)r^2\ .$$

The first two terms in $\phi_0$ are the external trap and space-charge potentials, given by Eqs. (2.4) and (2.9), respectively, and the last term is a pseudopotential due to rotation through the magnetic field.

We substitute Eqs. (5.1) into the cold-fluid equations [48] describing conservation of momentum and particle number, as well as into Poisson's equation. In the rotating frame, the cold-fluid equations have the same form as in an inertial frame (for example, the laboratory frame), except that the electrostatic potential is changed as indicated above and the cyclotron frequency is changed to the vortex frequency $\Omega_v=\Omega-2\omega_r$. When equilibrium force balance is taken into account and the equations are linearized in the small perturbations, we obtain the linearized continuity, momentum, and Poisson equations of cold-fluid theory:

$$\frac{\partial\delta n}{\partial t}+\nabla\cdot(n_0\delta\mathbf{v})=0\ , \tag{5.2a}$$

$$\frac{\partial\delta\mathbf{v}}{\partial t}+\frac{q}{m}\nabla\psi-\delta\mathbf{v}\times\Omega_v\hat{\mathbf{z}}=0\ , \tag{5.2b}$$

$$\nabla^2\psi=-\frac{q}{\epsilon_0}\delta n\ , \tag{5.2c}$$

where $\hat{\mathbf{z}}$ is a unit vector along the $z$ axis. Equation (5.2b) and further equations implicitly assume $q>0$. For $q<0,\Omega_v\rightarrow-\Omega_v$. Using the assumption that the perturbed quantities have a time dependence of the form $e^{-i\omega t}$ in the rotating frame (so that $\omega$ is the mode frequency as seen in this frame), a differential equation for $\psi$ follows from standard algebraic manipulations of Eqs. (5.2):

$$\nabla\cdot\boldsymbol{\epsilon}\cdot\nabla\psi=0\ , \tag{5.3a}$$

where $\boldsymbol{\epsilon}$ is the cold-plasma dielectric tensor. In Cartesian coordinates

$$\boldsymbol{\epsilon}=\begin{bmatrix}\epsilon_1 & -i\epsilon_2 & 0\\ i\epsilon_2 & \epsilon_1 & 0\\ 0 & 0 & \epsilon_3\end{bmatrix}\ , \tag{5.3b}$$

where $\epsilon_1\equiv1-\omega_p^2/(\omega^2-\Omega_v^2)$, $\epsilon_2\equiv\Omega_v\omega_p^2/[\omega(\omega^2-\Omega_v^2)]$, and $\epsilon_3\equiv1-\omega_p^2/\omega^2$. Equation (5.3a) is just Maxwell's equation $\nabla\cdot\mathbf{D}=0$ for a medium with a linear frequency-dependent anisotropic dielectric tensor $\boldsymbol{\epsilon}$. After a solution to Eqs. (5.2) for the perturbed potential $\psi$ is found, Eqs. (5.2) can be used to calculate the perturbed density $\delta n$ and perturbed fluid velocity $\delta\mathbf{v}$.

The normal mode problem requires a solution to Eq. (5.3) subject to the boundary condition that $\psi\rightarrow0$ at infinity, which is a problem in the theory of electrostatics. Outside the plasma $\boldsymbol{\epsilon}=1$ and $\psi$ satisfies Laplace's equation, $\nabla^2\psi^{\text{out}}=0$. Inside the plasma the dielectric tensor is anisotropic and the solution of Eq. (5.3a) is more compli-

cated. The inner and outer solutions must be matched across the plasma-vacuum boundary according to

$$\psi^{\text{in}}=\psi^{\text{out}}|_{\text{boundary}} , \tag{5.4a}$$

$$\hat{\mathbf{n}}\cdot\boldsymbol{\epsilon}\cdot\nabla\psi^{\text{in}}=\hat{\mathbf{n}}\cdot\nabla\psi^{\text{out}}|_{\text{boundary}} , \tag{5.4b}$$

where $\hat{\mathbf{n}}$ is a unit vector normal to the plasma-vacuum boundary.

Although the formulation of the problem as one in the theory of electrostatics is a step forward, simple solutions are generally available only in one of the standard geometries for which a separable solution exists, and this is not a standard geometry. The surface of the plasma is spheroidal, while the dielectric tensor is anisotropic with a different, cylindrical, symmetry. However, Ref. [29] showed that Eq. (5.3) does in fact have a separable solution in an unusual frequency-dependent coordinate system. This is the only known exact analytic solution for normal modes in a magnetized plasma of finite size. The solution for the mode potential is

$$\psi=\begin{cases} AQ_l^m(\xi_1/d)P_l^m(\xi_2)e^{i(m\phi-\omega t)} & \text{(outside plasma)} , \\ BP_l^m(\bar{\xi}_1/\bar{d})P_l^m(\bar{\xi}_2)e^{i(m\phi-\omega t)} & \text{(inside plasma)} , \end{cases} \tag{5.5}$$

where $A$ and $B$ are constants and $Q_l^m$ and $P_l^m$ are associated Legendre functions. Outside the plasma, the solution is expressed in terms of spheroidal coordinates [49] $(\xi_1,\xi_2,\phi)$ defined by the relations

$$x\equiv[(\xi_1^2-d^2)(1-\xi_2^2)]^{1/2}\cos\phi ,$$

$$y\equiv[(\xi_1^2-d^2)(1-\xi_2^2)]^{1/2}\sin\phi ,$$

$$z\equiv\xi_1\xi_2 .$$

The coordinate $\xi_1$ is a generalized distance coordinate taking the value $\xi_1\in[z_0,\infty)$ outside the cloud, $\xi_2$ is a generalized latitude in the range $[-1,1]$ and $\phi$ is the usual azimuthal angle. Surfaces of constant $\xi_1$ are confocal spheroids with the surface of the cloud defined by $\xi_1=z_0$, and surfaces of constant $\xi_2$ are confocal hyperboloids. The foci are a distance $2|d|$ apart, where $d^2\equiv z_0^2-r_0^2$. The coordinates $(\xi_1,\xi_2,\phi)$ become the usual spherical coordinates $(r,\cos\theta,\phi)$ when $z_0=r_0$.

Inside the cloud the coordinates $(\bar{\xi}_1,\bar{\xi}_2,\phi)$ are employed in order to obtain a separable solution. These coordinates are transformed spheroidal coordinates defined by the equations

$$x\equiv[(\bar{\xi}_1^2-\bar{d}^2)(1-\bar{\xi}_2^2)]^{1/2}\cos\phi ,$$

$$y\equiv[(\bar{\xi}_1^2-\bar{d}^2)(1-\bar{\xi}_2^2)]^{1/2}\sin\phi , \tag{5.6}$$

$$z(\epsilon_1/\epsilon_3)^{1/2}\equiv\bar{\xi}_1\bar{\xi}_2 .$$

where $\bar{d}^2\equiv\bar{z}_0^2-r_0^2$ and $\bar{z}_0\equiv z_0(\epsilon_1/\epsilon_3)^{1/2}$. These coordinates are frequency dependent; the different possible topologies of the coordinate surfaces are discussed in Ref. [29].

Returning to Eq. (5.5), we note that different normal modes are enumerated by the integers $l$ and $m$, where $l\geq 0$ and $|m|\leq l$. In fact, values of $m<0$ do not give rise to new modes if negative frequencies are allowed. Therefore $m\geq 0$ is assumed throughout, and negative frequencies are allowed. For $m\neq 0$, positive and negative frequency modes rotate about the $z$ axis in opposite directions. As discussed in Sec. III, we use the convention that modes with positive frequency rotate counterclockwise when viewed from above the $x$-$y$ plane (so that $d\phi/dt>0$ for $\omega>0$). The two directions of rotation are not equivalent due to the applied magnetic field. The mode frequencies for positively and negatively charged particles differ by a minus sign.

For a given pair $(l,m)$ the mode potential outside the cloud decays away like $s^{(-l-1)}$ at large distances $s$ from the cloud center [because $Q_l^m(x)\to x^{-(l+1)}$ for large $x$ and $\xi_1\to s$ for large $s$]. The modes can also be differentiated by the number of oscillations in $\psi$. For example, there are $l-m$ zeros in the potential as one moves in $\xi_2$ along a given spheroid outside the plasma from one pole to the other [that is, from $\xi_2=1$ to $-1$ on a constant $(\xi_1,\phi)$ curve]. This is because $P_l^m(x)$ has $l-m$ zeros in the range $[-1,1]$.

The variation of the potential outside the cloud is independent of the mode frequency, up to the overall constant $A$. However, inside the cloud, the frequency dependence of the coordinates (through their dependence on $\epsilon_1$ and $\epsilon_3$) implies that the behavior of the mode potential varies depending on the mode frequency, the plasma frequency and vortex frequency [except for two exceptional cases described in Eqs. (5.9) and (5.10) below]. This behavior can be understood qualitatively from the spatial Fourier transform of Eq. (5.3a),

$$\epsilon_1\mathbf{k}_\perp^2+\epsilon_3k_z^2=0 , \tag{5.7}$$

where $\mathbf{k}_\perp$ and $k_z$ are the components of the wave vector perpendicular and parallel to the magnetic field, respectively. When $\omega/\omega_p$ and $\Omega/\omega_p$ are such that $\epsilon_1/\epsilon_3<0$, a solution of this equation exists with both $\mathbf{k}_\perp$ and $k_z$ real, which is a propagating mode. However, when $\epsilon_1/\epsilon_3>0$, Eq. (5.7) implies that either $\mathbf{k}_\perp$ or $k_z$ must be imaginary and the mode is evanescent. The frequency dependence of the $\epsilon$'s implies that the propagating mode relation $\epsilon_1/\epsilon_3<0$ is satisfied by frequencies in the ranges $0<|\omega|<\min[\omega_p,|\Omega_v|]$ and $\max[\omega_p,|\Omega_v|]<|\omega|<\Omega_u$, where $\Omega_u=(\omega_p^2+\Omega_v^2)^{1/2}$ is the upper hybrid frequency. Modes in the first frequency range are called magnetized plasma oscillations, and modes in the second frequency range are called upper hybrid modes [50]. As we will see presently, evanescent modes occur only when $|\Omega_v|<\omega_p$, and such modes have frequencies in the range $|\Omega_v|<|\omega|<\omega_p$. These regimes are shown in Fig. 14 as a function of the rotation frequency. (Here, remember that both the vortex frequency and the plasma frequency are functions of $\omega_r$.) Modes with frequencies falling in areas labeled $A$ are magnetized plasma modes, modes falling in areas $B$ are upper hybrid modes, and modes falling in $C$ are evanescent.

Modes which are evanescent have a different potential variation within the cloud than modes which are propagating. Propagating modes reflect off the interior surface of the spheroid and set up a standing-wave pattern inside the cloud, whereas evanescent modes propagate along the cloud surface but decay with distance from the surface

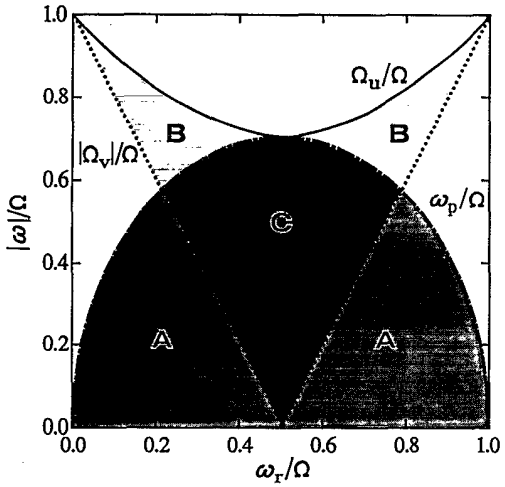


FIG. 14. Sketch showing the areas of allowed mode frequencies $\omega$ as a function of the rotation frequency $\omega_r$. Modes in regions *A*, *B*, and *C* are, respectively, magnetized plasma, upper hybrid, and evanescent modes.

into the plasma. (Because of the curvature of the cloud's surface, this decay is algebraic rather than the exponential decay we would observe for an evanescent mode at a planar interface.)

For example, the zeros of the (2,0) mode potential within the cloud are shown in Fig. 15 for the case of a spherical plasma with $\Omega_v/\omega_p=0.5$. As discussed in Secs. III and IV, there are two possible forms for the potential corresponding to a high-frequency upper hybrid mode [labeled (a)] and a lower-frequency mode [labeled (b)]. The upper hybrid mode is propagating, but for this value of $\Omega_v/\omega_p$ the lower-frequency mode is evanescent, decaying with distance into the plasma. This behavior is best observed in Figs. 15(c) and 15(d), which show the potential variation of the modes along $z=0$ and $r=0$, respectively.

Furthermore, either Fig. 15(a) or Figs. 15(c) and 15(d) show that the potential of the upper hybrid mode nearly vanishes along the cloud surface, so there is almost no potential variation exterior to the cloud. This is because as $\Omega_v/\omega_p\to 0$ (the Brillouin limit in a Penning trap or the condition for ions in a Paul trap) the upper hybrid modes have frequency $\omega=\omega_p$ and, as shown below, become bulk plasma oscillations with $\psi^{\text{out}}=0$. If $\Omega_v/\omega_p\to 0$ and $\omega\to\omega_p$, then $\epsilon=0$ and Eq. (5.4) implies $\nabla\psi^{\text{out}}\cdot\hat{\mathbf{n}}=0$ along the plasma boundary. The only solution which satisfies both the boundary condition at the plasma and $\psi^{\text{out}}\to 0$ at infinity is $\psi^{\text{out}}=0$. Furthermore in the $\Omega_v/\omega_p\to 0$ limit the magnetized plasma modes disappear as their frequency $\omega\to 0$. Thus, only the evanescent modes with $\epsilon_1/\epsilon_3>0$ may be observable near the $\Omega_v/\omega_p\to 0$ limit if only electrostatic detection of the modes is employed. In this limit the evanescent modes satisfy $\nabla^2\psi^{\text{in}}=0$, so from Eq. (5.2) there is no density perturbation except at the surface of the cloud. In this limit the evanescent modes induce incompressible deformations of the cloud's shape, and for this reason they are often called surface modes.

As a second example, the interior potential variation of the four possible (4,0) normal mode potentials are shown in Fig. 16, again for a spherical cloud with $\Omega_v/\omega_p=0.5$. Like the (2,0) modes, these modes could also be driven by in-phase oscillation of the end-cap potentials. There are now four zeros in the exterior potential as we move from pole to pole along the spheroid, as can be observed in Figs. 16(a)–16(d). Figures 16(a) and 16(b) correspond to upper hybrid modes, whereas Fig. 16(d) is a magnetized plasma mode and Fig. 16(c) is an evanescent mode. The decay of the evanescent mode with distance into the plas-

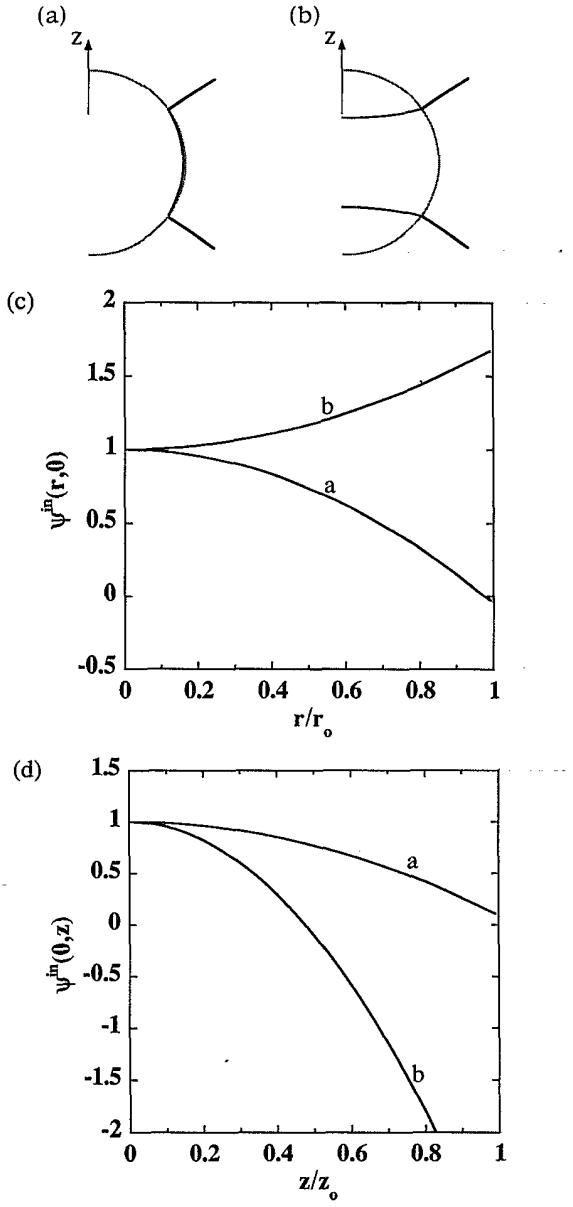


FIG. 15. (a) and (b) show the zeros of the potential for the two $l=2$, $m=0$ modes in a spherical plasma with $\Omega_v/\omega_p=0.5$. (a) is the upper hybrid mode and (b) is the plasma mode which is evanescent for these conditions. In (c) the variation of the mode potential (normalized to the potential at the plasma center) is shown as a function of cylindrical radius $r$ in the $z=0$ plane, and in (d) the potential is shown as a function of $z$ along $r=0$.

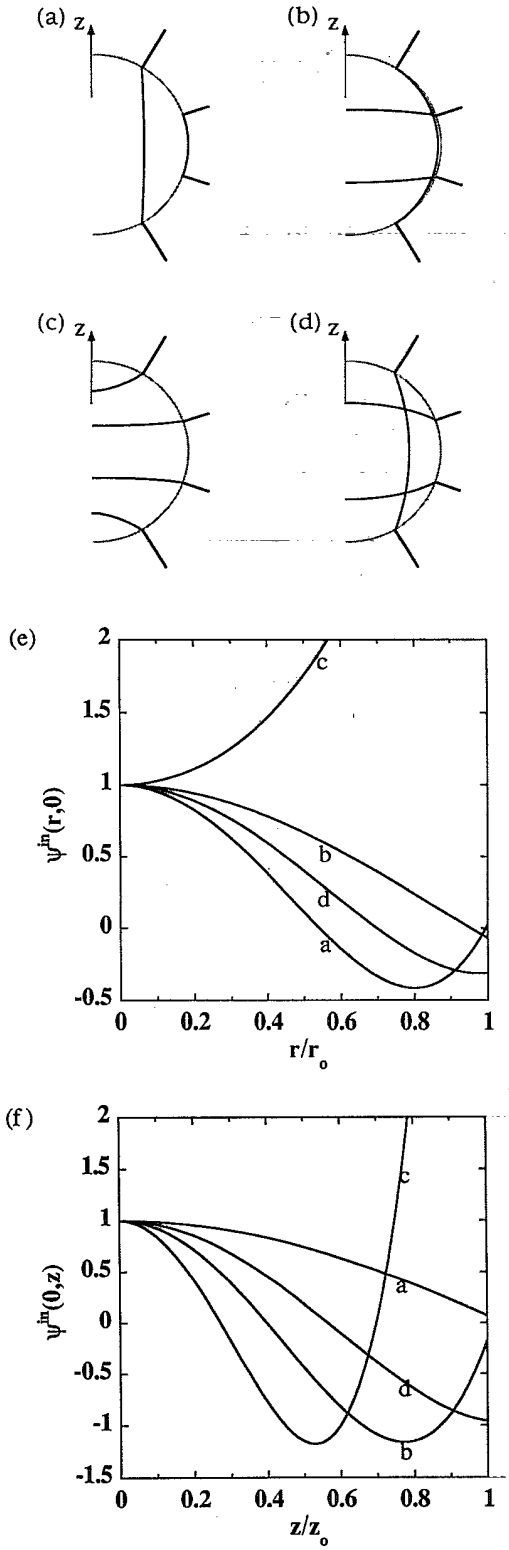


FIG. 16. (a)–(d) show the zeros of the potential for the four $l=4, m=0$ modes in a spherical plasma cloud with $\Omega_v/\omega_p=0.5$, in order of highest frequency (a) to lowest frequency (d). In (e) the variation of the mode potential (normalized to the potential at the plasma center) is shown as a function of cylindrical radius $r$ in the $z=0$ plane, and in (f) the potential is shown as a function of $z$ along $r=0$. The labels (a)–(d) correspond to Fig. 15(a)–15(d).

ma is most easily observed in Figs. 16(e) and 16(f). Just as with the (2,0) modes, for this relatively low value of $\Omega_v/\omega_p$ the upper hybrid modes induce almost no potential variation outside the cloud, as opposed to the magnetized plasma mode or the evanescent mode.

Finally, there are two exceptional cases for which the form of the mode potential is independent of $\omega$, $\omega_p$, and $\Omega_v$. When $l=m$ or $l=m+1$, we can substitute into Eq. (5.5) the general form of the Legendre function $P_l^m$,

$$P_l^m(x)=\sum_{j=0}^{(l-m)/2}(1-x^2)^{m/2}p_j x^{l-m-2j}, \tag{5.8}$$

where the $p_j$'s are given numbers, and use Eq. (5.6) to show that

$$\psi^{in}_{(m,m)}=\bar{A}r^m e^{i(m\phi-\omega t)} \tag{5.9}$$

and

$$\psi^{in}_{(m+1,m)}=\bar{B}r^m z e^{i(m\phi-\omega t)}, \tag{5.10}$$

where $\bar{A}$ and $\bar{B}$ are constants. (In fact, for all $l$ and $m$, $\psi^{in}$ can be expressed as a finite-order multinomial in $x$, $y$, and $z$.) In the cases of Eqs. (5.9) and (5.10) the form of the mode potential is independent of $\omega$, $\omega_p$, and $\Omega_v$, because the mode satisfies $\partial^2\psi^{in}/\partial z^2=0$ and $\nabla_\perp^2\psi^{in}=0$ separately, and so Eq. (5.3a) is satisfied for any $\epsilon_1$ and $\epsilon_3$. Furthermore, these particular modes satisfy $\nabla^2\psi^{in}=0$, so they cause incompressible deformations of the cloud for all $\omega_p$ and $\Omega_v$; that is, they are always surface modes. For example, for the case of the (2,1) mode, $\psi^{in}_{(2,1)}=\bar{B}e^{i(\phi-\omega t)}rz$, which is the potential inside a tilted cloud precessing at frequency $\omega$, in agreement with the analysis of Sec. III. The (1,0) and (1,1) modes are also examples of incompressible cloud deformations, which correspond to the well-known axial center-of-mass and magnetron modes.

The (2,2) mode is an incompressible distortion of the cloud into a triaxial ellipsoid, leaving the length of the cloud fixed at $2z_0$. In general, the $(l,l)$ modes are finite length extensions of the $z$-independent diocotron and upper hybrid surface modes of cylindrical non-neutral plasmas [51].

Although the $l=m$ and $l=m+1$ surface modes appear to be fundamentally different from other magnetized plasma, upper hybrid, and evanescent modes, in fact they display many characteristics which are similar to these modes. For example, when $\omega_r \ll \Omega$ two of the three (2,1) oscillations can be thought of as finite length versions of magnetized plasma modes in a cylindrical column. The modes (indicated by the upper two curves in Fig. 8) have $m=1$ and a half wavelength potential variation over the length of the column; they rotate in opposite directions around the column. Similarly, the other (2,1) mode is a finite length version of an upper hybrid oscillation which also has a half wavelength variation over the column length. Modes with larger values of $l$ simply have more wavelengths fitted into the column length, and so are not fundamentally different. Indeed, we will soon see that the frequencies of these $l=m$ and $l=m+1$ modes behave in a qualitatively similar fashion as those of the other propagating and evanescent modes. When discussing the gen-

eral frequency dependence of the modes, we therefore do not need to make a distinction between these modes and modes with other values of $l$ and $m$.

Turning now to the normal mode frequencies, Ref. [29] showed that substitution of Eq. (5.5) into Eq. (5.4) leads to two homogeneous linear equations for $A$ and $B$ which have a nontrivial solution only if

$$\epsilon_3 P_l^{m'} + m\alpha \left[ \alpha^2 - \frac{\epsilon_3}{\epsilon_1} \right]^{1/2} P_l^m \epsilon_2 - \left[ \frac{\alpha^2 - \epsilon_3/\epsilon_1}{\alpha^2 - 1} \right]^{1/2} P_l^m \frac{Q_l^{m'}}{Q_l^m} = 0 . \quad (5.11)$$

Here $P_l^m \equiv P_l^m(\alpha/(\alpha^2-\epsilon_3/\epsilon_1)^{1/2})$, $Q_l^m \equiv Q_l^m(\alpha/(\alpha^2-1)^{1/2})$, $\alpha \equiv z_0/r_0$, and the primes denote differentiation with respect to the entire argument.

The general behavior of the solutions to this equation was considered in Ref. [29]. Here, we discuss a simplification of Eq. (5.11) which aids in the determination of the solutions, and we consider some examples. Analysis of the roots of this nonlinear equation is aided by the fact that it can be expressed as a polynomial in the frequency $\omega$. This polynomial can be derived by substitution of Eq. (5.8) into Eq. (5.11), which leads, after some algebra, to the expression

$$x^{l-m-1}(1-x^2)^{m/2} \sum_{j=0}^{(l-m)/2} p_j x^{-2j} \left[ m\alpha^2(\epsilon_1+\epsilon_2) + (l-m-2j)\epsilon_3 - \frac{\alpha}{(\alpha^2-1)^{1/2}} \frac{Q_l^{m'}}{Q_l^m} \right] = 0 , \quad (5.12)$$

where $x = \alpha/(\alpha^2-\epsilon_3/\epsilon_1)^{1/2}$. The factor before the sum is nonzero and can be discarded. Furthermore, since $x^{-2j} = (1-\epsilon_3/\alpha^2\epsilon_1)^j$, and $\epsilon_1$, $\epsilon_2$, and $\epsilon_3$ are rational functions of $\omega$, the sum itself may be expressed as a polynomial in $\omega$. For example, $\epsilon_3/\epsilon_1 = (\omega^2-\Omega_v^2)(\omega^2-\omega_p^2)/[\omega^2(\omega^2-\Omega_u^2]$, and $\epsilon_1+\epsilon_2 = (\omega^2+\omega\Omega_v-\omega_p^2)/[\omega(\omega+\Omega_v)]$. Substitution of these results into Eq. (5.12) leads, after some further reduction, to the following polynomial equation:

$$\sum_{j=0}^{(l-m)/2} a_j b^j c^{\mathrm{int}[(l-m)/2]-j} = 0 , \quad (5.13)$$

where

$$a_j \equiv p_j \left[ (\omega+\Omega_v) \left[ (l-m-2j)(\omega^2-\omega_p^2) - \frac{\alpha}{(\alpha^2-1)^{1/2}} \frac{Q_l^{m'}}{Q_l^m} \omega^2 \right] + m\alpha^2\omega(\omega^2-\omega_p^2+\omega\Omega_v) \right] ,$$

$$b \equiv \alpha^2\omega^2(\omega^2-\Omega_u^2) - (\omega^2-\omega_p^2)(\omega^2-\Omega_v^2) ,$$

and

$$c \equiv \alpha^2\omega^2(\omega^2-\Omega_u^2) .$$

The function int$[(l-m)/2]$ denotes the largest integer less than or equal to $(l-m)/2$.

This form of the dispersion relation (the dependence of $\omega$ on $\alpha$ for a given $l,m$) is considerably more simple to solve numerically than Eq. (5.12), using any polynomial-root-finding algorithm. Furthermore, the equation leads to some simple analytic results. For example, we can count the number of normal modes by determining the order of the polynomial. The order is $3+4\,\mathrm{int}[(l-m)/2]$; however, we must be careful to exclude any spurious roots generated in the derivation of Eq. (5.13) through multiplication by resonant denominators of $\epsilon_1$, $\epsilon_2$, or $\epsilon_3$. When $m=0$ and $l$ is odd, there is a single spurious root at $\omega=-\Omega_v$ [due to the $(\omega+\Omega_v)$ term in $a_j$]. If $m=0$ and $l$ is even there are three spurious roots at $\omega^2=0$ and $\omega=-\Omega_v$. Subtracting out these roots from the total, we find for $m=0$ there are $2l$ normal modes. However, when $m=0$, Eq. (5.13) is a polynomial of order $l$ in $\omega^2$. The roots then come in $l$ pairs at $\pm\omega$, and the pairs do not really correspond to two separate modes; indeed, Eq. (5.5) shows that the mode potential is identical for both $\pm\omega$ when $m=0$.

When $m\neq 0$ and when $l-m$ is even, there is a single spurious root at $\omega=0$, while when $l-m$ is odd, there are no spurious roots. Thus, when $l-m$ is even there are $[2(l-m)+2]$ modes, and when $l-m$ is odd there are $[2(l-m)+1]$ modes. The roots no longer come in $\pm\omega$ pairs because, for $m\neq 0$, modes with positive and negative frequencies rotate in opposite directions around the $z$ axis, and these directions are not equivalent because of the magnetic field.

Some simple analytic results are also possible for the mode frequencies when $l=m$ or $l=m+1$. In this case only the $j=0$ term survives from Eq. (5.13) and the modes are determined by the equation $a_0=0$. When $l=m$ this is a quadratic equation with roots given by

$$\omega_{l,l} = -\Omega_v/2 \pm \sqrt{\Omega_v^2/4+\omega_p^2/[1-(r_0/l\alpha d)Q_l^{l\prime}/Q_l^l]} . \quad (5.14)$$

For $\Omega_v>0$ the low-frequency mode (upper sign) corresponds to the diocotron mode of a cylindrical non-neutral plasma [51] and the high-frequency mode (lower sign) is a

surface mode in the upper hybrid frequency regime.

When $l=m+1$, Eq. (5.13) becomes

$$(\alpha_l+\beta_l)\omega^2(\omega+\Omega_v)-\alpha_l\omega\omega_p^2-\Omega_v\omega_p^2=0\ , \qquad (5.15)$$

where $\alpha_l\equiv 1+\alpha^2(l-1)$ and $\beta_l\equiv-[\alpha/(\alpha^2-1)^{1/2}]Q_l^{l-1'}/Q_l^{l-1}$. There are three solutions for the mode frequency which, when $l=2$, are the same as the solutions of Eqs. (3.22)–(3.24) for the (2,1) mode. When $l=1$, one of the roots is spurious and the other two approach the single-particle axial bounce frequency $\omega_z=\omega_p/(1+\beta_1)^{1/2}$ in agreement with Eq. (2.6); this is the axial center-of-mass mode.

Results for the frequencies when $l=m+2$, $m+3$, ... require the solution of even higher-order polynomial equations. We have found the solutions numerically, and some results are displayed in Figs. 17(a)–17(c) as functions of the rotation frequency $\omega_r$. It is important to remember here that both $\Omega_v$ and $\omega_p$ are functions of the $\omega_r$; in fact, in the rotating frame the plasma becomes unmagnetized at the Brillouin limit $\Omega_v=0$.

Examination of the mode frequencies at the Brillouin limit (equivalent to the case of ions in a Paul trap) shows that for given $l$ and $m$ there are two modes which become unmagnetized surface plasma oscillations. These surface mode frequencies are described by the particularly simple limiting form of Eq. (5.11), $\epsilon_3=P_l^mQ_l^{m'}/P_l^{m'}Q_l^m$ [here the argument of the $P_l^m$'s simplifies to $\alpha/(\alpha^2-1)^{1/2}$]. Thus, when $\Omega_v=0$ there are a pair of surface modes with frequencies of opposite sign. For $\Omega_v\neq 0$ but $|\Omega_v|<\omega_p$ and $l\to\infty$, these modes are evanescent, approaching the magnetized surface plasma frequencies $\pm\Omega_u/\sqrt{2}$. This result is independent of the shape of the cloud. However, for $|\Omega_v|>\omega_p$ the behavior of these two modes depends on $m$. When $m=0$ the pair of modes remains in the magnetized plasma regime $\omega<\omega_p$, as shown in Figs. 17(b) and 17(c). When $m\neq 0$, however, only one mode remains in the magnetized plasma regime, while the other enters the upper hybrid range, as shown in Fig. 17(a).

The rest of the modes always remain in either the magnetized plasma or upper hybrid regime. Their numbers are as follows; when $m\neq 0$ there are $l-m$ magnetized plasma modes and $2\,\mathrm{int}[(l-m)/2]$ upper hybrid modes; when $m=0$ there are $\mathrm{int}[(l-1)/2]$ pairs of magnetized plasma modes, and $\mathrm{int}[l/2]$ pairs of upper hybrid modes. [These numbers can be determined by analysis of the solutions of Eq. (5.13) in the limits $\Omega_v\to\infty$ and $\Omega_v\to 0$.]

Finally, we compare the frequencies of (2,0) and (4,0) modes, which, like the (2,0) modes, can be excited using the technique described in Sec. IV. The frequency of the evanescent (4,0) mode, shown in Fig. 17(b) for the experimental value $\omega_z/\Omega=0.151$, is quite different from the evanescent (2,0) frequency, which was measured experimentally. Evanescent branches with higher $l$ are even further removed from the $l=2$ root, approaching $\Omega_u/\sqrt{2}$. This provides further evidence that the measured mode shown in Fig. 12 is in fact a (2,0) mode excitation and not a higher-order oscillation. However, it should be possible to excite other $m=0$ even $l$ modes using the same experimental technique. For larger values of $\omega_z/\Omega$, however, the evanescent (2,0) mode becomes

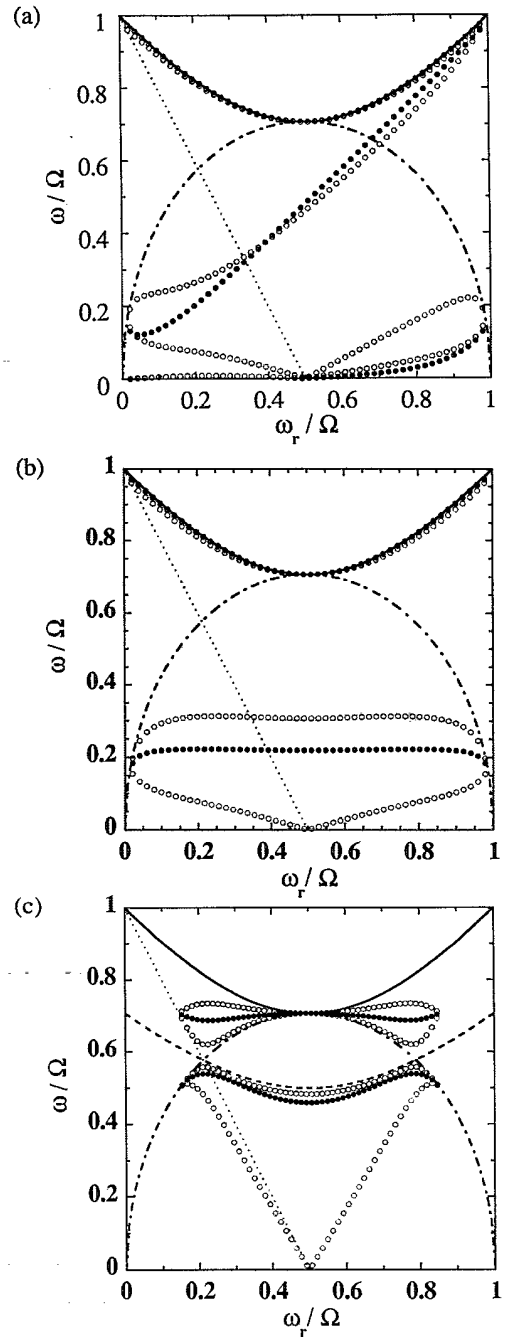


FIG. 17. Mode frequencies $\omega$ in the rotating frame vs rotation frequency $\omega_r$ for different values of $(l,m)$ and $\omega_z$. (From Sec. V B, $\omega^{\mathrm{lab}}=\omega-m\omega_r$.) For $\omega<0$ the diagrams should be reflected through the point $(\omega_r,\omega)=(\Omega/2,0)$. Also shown for comparison are the upper hybrid frequency $\Omega_u(\omega_r)$ (solid curve), the vortex frequency $\Omega_v(\omega_r)$ (dotted curve), the plasma frequency $\omega_p(\omega_r)$ (dot-dashed curve), and in (c) the surface upper hybrid frequency $\Omega_u(\omega_r)/\sqrt{2}$ (dashed curve). All frequencies are expressed in units of the cyclotron frequency $\Omega$. (a) $\omega_z/\Omega=0.151$; $(l,m)=(2,1)$, filled circles; $(l,m)=(5,1)$, open circles. The (2,1) modes for this condition are also shown in Fig. 8 in the laboratory frame. (b) $\omega_z/\Omega=0.151$; $(l,m)=(2,0)$, filled circles; $(l,m)=(4,0)$, open circles. The (2,0) modes for this condition are also shown in Fig. 6. They are the same in the laboratory or rotating frame. (c) $\omega_z/\Omega=0.5$; $(l,m)=(2,0)$, filled circles; $(l,m)=(4,0)$, open circles.

nearly degenerate with the evanescent (4,0) mode [see Fig. 17(c)], making it more difficult to distinguish between modes with different values of $l$ merely from frequency measurements.

### B. Resonances between modes and static field errors

Now that the linear modes have been enumerated, we turn to the problem of modes driven by an external source. In particular, as we saw in Sec. IV, a static field error can drive to large amplitude a (2,1) mode, when the mode satisfies the linear resonance condition that it has zero frequency in the laboratory frame. In this section we consider the resonance between a static error and modes with general $(l,m)$.

In the rotating frame, modes have a variation proportional to $\exp(im\phi - i\omega t)$. The azimuthal angle $\phi$ as viewed in the rotating frame is related to the angle $\phi_L$ as viewed in the laboratory frame through the Galilean transformation $\phi = \phi_L + \omega_r t$. Therefore, the condition that a mode has zero frequency in the laboratory frame is

$$\omega = m\omega_r \ . \tag{5.16}$$

Solutions of this equation can be found graphically in Fig. 17 by finding the intersections of the line given by Eq. (5.16) and the curves of mode frequency versus rotation frequency. In general, for a given $l$ and $m$ there are $l-m$ intersections for $m \neq 0$ and no intersections when $m=0$. [Equation (5.16) implicitly assumes $m \geq 0$ and positively charged, trapped particles as discussed earlier. With the sign convention used here where $\omega_r$ is always positive, the condition for negatively charged particles is $\omega = -m\omega_r$.]

For a given $\omega_z/\Omega$ the solutions of Eq. (5.16) provide specific values of $\omega_r/\Omega$ at which resonances can occur between a static error and a mode with given $(l,m)$. These values trace out curves as $\omega_z/\Omega$ is varied; the curves are plotted for $m=1$ and $m=2$ in Fig. 18. Since modes with $l-m$ odd are odd in $z$, these modes will be excited (in linear theory) only by errors which are also odd in $z$, such as the error induced by a tilt of the electrodes with respect to the magnetic field. Similarly, errors which are even in $z$ excite modes with $l-m$ even. Furthermore, only modes with the same value of $m$ as the perturbation can be excited (in linear theory). This implies that the tilt field error, which (for small tilt angles) is

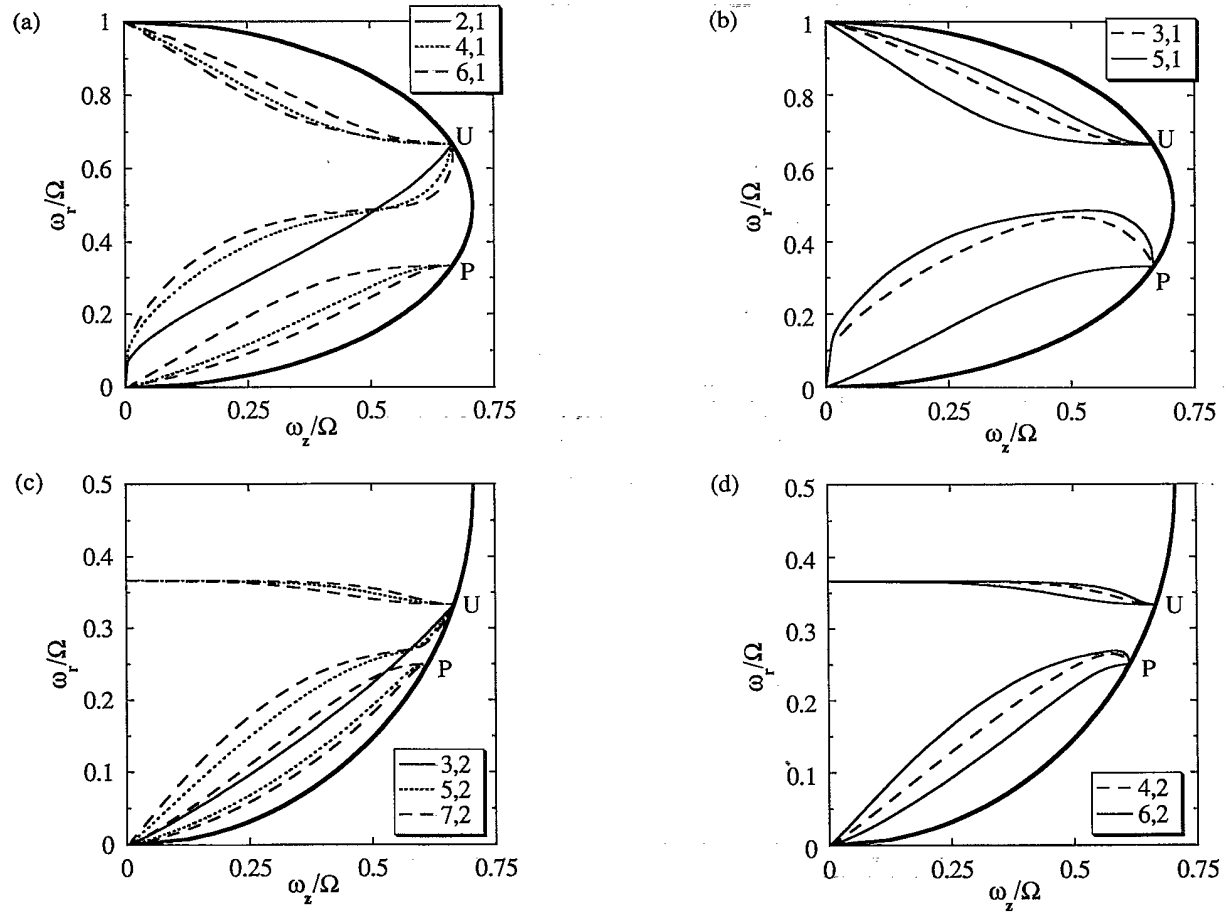


FIG. 18. Values of $\omega_r/\Omega$ and $\omega_z/\Omega$ for which different $m=1$ and $m=2$ modes become zero frequency in the laboratory frame. The limiting points $U$ and $P$, which fall on the confinement boundary, are discussed in the text. The confinement boundary, defined by $\omega_r=\omega_m$ and $\omega_r=\Omega-\omega_m$, where $\omega_m$ is given by Eq. (2.10), is also drawn. The $m=1$ modes are shown in (a) and (b), and the $m=2$ modes are shown in (c) and (d). Modes odd in $z$ are shown in (a) and (c) and modes even in $z$ are shown in (b) and (d). The curve for the zero-frequency (2,1) mode in (a) is the curve in Fig. 10.

an $m=1$ perturbation that is odd in $z$, can linearly resonate only with the (2,1), (4,1), (6,1), . . . modes.

The (2,1) mode is most strongly excited since it has the slowest spatial variation and hence has the largest "overlap" with the slowly varying tilt error. Furthermore, the (4,1) and (6,1) resonance curves have quite different forms from the (2,1) curve, which indicates that the excitation observed in the experiments is in fact a (2,1) mode, not a higher-order excitation. However, the other resonances may also be measurable.

Turning now to the limiting behavior of the resonance curves, we observe that in the rotating-frame mode frequencies are always less than the upper hybrid frequency $\Omega_u=(\omega_p^2+\Omega_v^2)^{1/2}$. Then Eq. (5.16) implies that resonant rotation frequencies must satisfy the relation

$$m\omega_r \leq \sqrt{\omega_p^2+\Omega_v^2}=\sqrt{2\omega_r(\Omega-\omega_r)+(\Omega-2\omega_r)^2}\ ,$$

which can be solved to give

$$\omega_r/\Omega \leq (\sqrt{m^2-1}-1)/(m^2-2)=1,0.366,0.261,\ldots\ .$$

This implies that as $m$ increases the resonances become packed into a smaller and smaller region of the experimental operating regime. Since most experiments operate in the regime $\omega_r/\Omega \ll 1$, we may have cause to worry that these many resonances could have a deleterious effect on the plasma confinement. However, the mode resonances with smaller values of $l$ and $m$ are most dangerous since they are more easily excited by perturbations with slow spatial variation, and larger $l$ and $m$ modes may be heavily damped due to viscous effects or collisionless Landau damping [52].

Other limiting values of the resonance curves can also be found. For example, consider the limit in which the plasma becomes extremely oblate, that is, a thin disk or pancake. This occurs along the edge of the confinement region defined by the equations $\omega_r=\omega_m$ and $\omega_r=\Omega-\omega_m$, where $\omega_m$ is given by Eq. (2.10). In this limit, the mode frequencies approach either $\Omega_v$ or $\omega_p$. In the former case resonances occur when $\Omega_v=m\omega_r$, or

$$\omega_r/\Omega=1/(m+2)=\tfrac{1}{3},\tfrac{1}{4},\tfrac{1}{5},\ldots\ .$$

This limit is labeled by the point $P$ in Fig. 18. In the latter case resonances occur when $\omega_p=m\omega_r$, which can be solved for $\omega_r$ to yield

$$\omega_r/\Omega=2/(m^2+2)=\tfrac{2}{3},\tfrac{1}{3},\tfrac{2}{11},\ldots\ .$$

This limit is labeled by the point $U$. Resonance curves which connect to the point $P$ are due to magnetized plasma modes, whereas curves connecting to point $U$ are due to resonances with upper hybrid modes.

Finally, we briefly discuss how the strength of these resonances should behave as the size or density of the plasma increases. Since the plasma is generally small compared to the distance to the electrodes, external field errors have slow spatial variation compared to the plasma size, and hence only the lowest-order $l$ and $m$ resonances should be observed. However, as the plasma increases in size higher-order modes have a larger "overlap" with the field error. Furthermore, as either plasma size or density is increased more electrostatic energy is liberated by radial expansion of the plasma due to the torque of the error acting on the cloud. Thus, we expect heating due to resonances to increase as more ions are trapped, and more resonances with higher values of $l$ and $m$ should be observable. This qualitative picture appears to agree with observations of higher density ion clouds. However, a quantitative analysis of this important question involves effects which are beyond the scope of this work, such as the effect of viscosity, Landau damping, laser light pressure, and nonlinearities on the saturation level of the mode amplitude. These issues need to be considered in a future paper.

## ACKNOWLEDGMENTS

We thank John Schiffer for stimulating discussions on this subject and Steve Jefferts and Steve Barlow for their comments and careful reading of the manuscript. We gratefully acknowledge support by the U.S. Office of Naval Research Contract No. N00014-92-F-0038. D.H.E.D. acknowledges the support of the U.S. Office of Naval Research Contract No. N00014-89-J-1714 as well as National Science Foundation Grants No. PHY87-06358 and No. PHY91-20240.

*Current address: Department of Physics, University of Texas, Austin, TX 78712.

[1] H. G. Dehmelt, Adv. At. Mol. Phys. **3**, 53 (1967); **5**, 109 (1969); D. J. Wineland, W. M. Itano, and R. S. Van Dyck, Jr., *ibid.* **19**, 135 (1983); R. C. Thompson, Adv. At. Mol. Opt. Phys. (to be published).

[2] J. H. Malmberg and J. S. deGrassie, Phys. Rev. Lett. **35**, 577 (1975).

[3] M. L. Gross and D. L. Rempel, Science **226**, 261 (1984); A. G. Marshall, Acc. Chem. Res. **18**, 316 (1985).

[4] R.S. Van Dyck, Jr., P. B. Schwinberg, and S. H. Bailey, in *Atomic Masses and Fundamental Constants 6,* edited by J.A. Nolan, Jr. and W. Benenson (Plenum, New York, 1980), p. 173; R. S. Van Dyck, Jr., D. L. Farnham, and P. B. Schwinberg, Phys. Scr. **46**, 257 (1992).

[5] E. A. Cornell, R. M. Weisskoff, K. R. Boyce, R. W. Flanagan, Jr., G. P. Lafyatis, and D. E. Pritchard, Phys. Rev. Lett. **63**, 1674 (1989).

[6] G. Bollen, R. B. Moore, G. Savard, and H. Stolzenberg, J. Appl. Phys. **68**, 4355 (1990).

[7] G. Gabrielse, X. Fei, L. A. Orozco, R. L. Tjoelker, J. Hass, H. Kalinowsky, T. A. Trainor, and W. Kells, Phys. Rev. Lett. **65**, 1317 (1990).

[8] D. Hagena and G. Werth, Europhys. Lett. **15**, 491 (1991); J. Kern, T. Engel, D. Hagena, and G. Werth, Phys. Scr. **46**, 575 (1992).

[9] R. S. Van Dyck, Jr., P. B. Schwinberg, and H. G. Dehmelt, Phys. Rev. D **34**, 722 (1986); Phys. Rev. Lett. **59**, 26 (1987).

[10] M. Hubrich, H. Knab, K. H. Knoell, and G. Werth, Z. Phys. D **18**, 113 (1991).

[11] *Frequency Standards and Metrology,* Proceedings of the

Fourth Symposium on Frequency Standards and Metrology, Ancona, Italy, edited by A. De Marchi (Springer-Verlag, Berlin, 1989).

[12] J. J. Bollinger, D. J. Heinzen, W. M. Itano, S. L. Gilbert, and D. J. Wineland, Phys. Rev. Lett. **63**, 1031 (1989); J. J. Bollinger *et al.*, IEEE Trans. Instrum. Meas. **40**, 126 (1991); D. J. Wineland, *et al.*, IEEE Trans. Ultrason. Ferroelectrics Freq. Control **37**, 515 (1990).

[13] J. D. Prestage, G. J. Dick, and L. Maleki, IEEE Trans. Instrum. Meas. **40**, 132 (1991); L. S. Cutler, R. P. Giffard, P. J. Wheeler, and G. M. R. Winkler, in *Proceedings of the Forty-First Annual Frequency Symposium,* IEEE Catalog No. 87CH2427-3 (IEEE, New York, 1987), p. 12 (copies are available from NTIS, 5285 Port Royal Rd., Springfield, VA 22161); M. Jardino, M. Desaintfuscien, R. Barillet, J. Viennet, P. Petit, and C. Audoin, Appl. Phys. **24**, 107 (1981).

[14] A. Muench, M. Berkler, Ch. Gerz, D. Wilsdorf, and G. Werth, Phys. Rev. A **35**, 4147 (1987).

[15] D. A. Church, in *Physics of Electronic and Atomic Collisions,* edited by S. Datz (North-Holland, Amsterdam, 1982), p. 533; D. A. Church *et al.*, Nuclear Instrum. Methods Phys. Res. Sect. B **56/57**, 417 (1991).

[16] J. H. Malmberg, C. F. Driscoll, B. Beck, D. L. Eggleston, J. Fajans, K. Fine, X.-P. Huang, and A. W. Hyatt, in *Non-Neutral Plasma Physics,* Proceedings of the Symposium on Non-Neutral Plasma Physics, edited by C. W. Roberson and C. F. Driscoll, AIP Conf. Proc. No. 175 (AIP, New York, 1988), p. 28.

[17] C. F. Driscoll and K. S. Fine, Phys. Fluids B **2**, 1359 (1990).

[18] C. F. Driscoll, J. H. Malmberg, and K. S. Fine, Phys. Rev. Lett. **60**, 1290 (1988).

[19] D. L. Eggleston, T. M. O'Neil, and J. H. Malmberg, Phys. Rev. Lett. **53**, 982 (1984); D. L. Eggleston and J. H. Malmberg, *ibid.* **59**, 1675 (1987).

[20] S. L Gilbert, J. J. Bollinger, and D. J. Wineland, Phys. Rev. Lett. **60**, 2022 (1988).

[21] D. J. Heinzen, J. J. Bollinger, F. L. Moore, W. M. Itano, and D. J. Wineland, Phys. Rev. Lett. **66**, 2080 (1991); **66**, 3087E (1991).

[22] P. B. Schwinberg, R. S. Van Dyck, Jr., and H. G. Dehmelt, Phys. Lett. **81A**, 119 (1981).

[23] C. M. Surko, M. Leventhal, and A. Passner, Phys. Rev. Lett. **62**, 901 (1989).

[24] G. Gabrielse, X. Fei, L.A. Orozco, R. L.Tjoelker, J. Hass, H. Kalinowsky, T. A. Trainor, and W. Kells, Phys. Rev. Lett. **63**, 1360 (1989); **65**, 1317 (1990).

[25] R. S. Van Dyck, Jr. and P. B. Schwinberg, Phys. Rev. Lett. **47**, 395 (1981); R. S. Van Dyck, Jr., F. L. Moore, D. L. Farnham, and P. B. Schwinberg, Int. J. Mass Spectrom. Ion Processes **66**, 327 (1985).

[26] R. S. Van Dyck, Jr., F. L. Moore, D. L. Farnham, and P. B. Schwinberg, Phys. Rev. A **40**, 6308 (1989).

[27] F. L. Walls and G. H. Dunn, J. Geophys. Res. **79**, 1911 (1974); R. A. Heppner, F. L. Walls, W. T. Armstrong, and G. H. Dunn, Phys. Rev. A **13**, 1000 (1976).

[28] L. R. Brewer, J. D. Prestage, J. J. Bollinger, W. M. Itano, D. J. Larson, and D. J. Wineland, Phys. Rev. A **38**, 859 (1988).

[29] D. H. E. Dubin, Phys. Rev. Lett. **66**, 2076 (1991).

[30] S. A. Prasad and T. M. O'Neil, Phys. Fluids **22**, 278 (1979).

[31] D. H. E. Dubin and T. M. O'Neil, Phys. Rev. Lett. **60**, 511 (1988).

[32] J. H. Malmberg and T. M. O'Neil, Phys. Rev. Lett. **39**, 1333 (1977).

[33] D. J. Wineland, J. J. Bollinger, W. M. Itano, and J. D. Prestage, J. Opt. Soc. Am. B **2**, 1721 (1985).

[34] P. M. Morse and H. Feshbach, *Methods of Theoretical Physics* (McGraw-Hill, New York, 1963), Chap. 10.

[35] J. B. Jeffries, S. E. Barlow, and G. H. Dunn, Int. J. Mass Spectrom. Ion Processes **54**, 169 (1983).

[36] R. C. Davidson, in *Non-Neutral Plasma Physics* [16], p. 139.

[37] J. S. deGrassie and J. H. Malmberg, Phys. Fluids **23**, 63 (1980).

[38] S. A. Prasad and T. M. O'Neil, Phys. Fluids **26**, 665 (1983).

[39] R. Keinigs, Phys. Fluids **24**, 860 (1981); **27**, 1427 (1984).

[40] D. J. Wineland, J. C. Bergquist, M. W. Itano, and R. E. Drullinger, Opt. Lett. **5**, 245 (1980).

[41] H. S. Lakkaraju and H. A. Schuessler, J. Appl. Phys. **53**, 3967 (1982).

[42] D. J. Wineland, J. J. Bollinger, and W. M. Itano, Phys. Rev. Lett. **50**, 628 (1983); **50**, 1333E (1983).

[43] W. M. Itano, L. R. Brewer, D. J. Larson, and D. J. Wineland, Phys. Rev. A **38**, 5698 (1988).

[44] C. F. Driscoll, in *Low Energy Antimatter,* edited by David Cline (World Scientific, Singapore, 1986), pp. 184–195.

[45] J. Yu, M. Desaintfuscien, and F. Plumelle, Appl. Phys. B **48**, 55 (1989).

[46] C. F. Driscoll and J. H. Malmberg, Phys. Rev. Lett. **50**, 167 (1983).

[47] L. S. Cutler, C. A. Flory, R. P. Giffard, and M. D. McGuire, Appl. Phys. B **39**, 251 (1986); L. S. Cutler, R. P. Giffard, and M. D. McGuire, *ibid.* **36**, 137 (1985).

[48] R. C. Davidon, *Theory of Nonneutral Plasmas* (Benjamin, Reading, MA, 1974), pp. 14–16, and 43.

[49] P. M. Morse and H. Feshbach, *Methods of Theoretical Physics* (McGraw-Hill, New York, 1963), Chap. 5.

[50] F. F. Chen, *Introduction to Plasma Physics* (Plenum, New York, 1974), pp. 88–94.

[51] R. C. Davidson, *Theory of Nonneutral Plasmas* [48], p. 62.

[52] N. A. Krall and A. W. Trivelpiece, *Principles of Plasma Physics* (San Francisco Press, San Francisco, 1986), p. 386.